

CRANFIELD UNIVERSITY

XIUYUAN YANG

THE STUDY OF INFLUENCE FACTORS IN X-RAY COMPUTED  
TOMOGRAPHY USING SIMULATION APPROACH

School of Aerospace, Transport and Manufacturing  
MASTER OF RESEARCH IN MANUFACTURING

Master of Research  
Academic Year: 2017 - 2018

Supervisor: Dr Claudiu Giusca  
Co-Supervisor: Dr Wenjuan Sun  
08/2018



CRANFIELD UNIVERSITY

School of Aerospace, Transport and Manufacturing  
MASTER OF RESEARCH IN MANUFACTURING

MRes

Academic Year 2017 - 2018

XIUYUAN YANG

THE STUDY OF INFLUENCE FACTORS IN X-RAY COMPUTED  
TOMOGRAPHY USING SIMULATION APPROACH

Supervisor: Dr Claudiu Giusca  
Co-Supervisor: Dr Wenjuan Sun (NPL)  
08/2018

This thesis is submitted in partial fulfilment of the requirements for  
the degree of Master of Research

© Cranfield University 2018. All rights reserved. No part of this  
publication may be reproduced without the written permission of the  
copyright owner.



## **ABSTRACT**

XCT simulation scanning was used throughout the study because simulation scanning has the flexibility in changing scanning parameters as well as improving the efficiency. The research investigated the effect of voltage, scattering-contamination and multi-sampling on the quality of 2D image projection. For The study tested factors of scattering-contamination, multi-sampling and cone-beam angle on dimensional measurement error with the numerical geometry samples including spheres, cubes, cylinders and tubes. For cylinders and tubes, the measurement of outer diameter leaded more deviation than inner diameter. Scattering contamination had limited influencing (up to 1/35 of the voxel size) to the measurement result but scattering contamination can amplify the operator factor in the geometry determination step. 3X3 multi-sampling detector could optimise the measurement result when measuring the diameter of the cylinder. On the other hand, the effectiveness of the application of multi-sampling is related to the geometry features for measure, and the effect is independent to the scattering-contamination. When measuring circles on the tube, the cone-beam angle had only slight influence (up to 1/131 of voxel size) on the measurement error.

Keywords:

Cone beam angle, multi-sampling, scattering, sphere, Additive Manufacturing, voltage, current



## **ACKNOWLEDGEMENTS**

The project is supervised by Dr Claudiu Giusca from Cranfield University and Dr Wenjuan Sun from National Physical Laboratory. The author is grateful to the National Measurement System Programme for Engineering & Flow Metrology for the financial support to this project.





# TABLE OF CONTENTS

ABSTRACT .....	i
ACKNOWLEDGEMENTS.....	iii
LIST OF FIGURES .....	vii
LIST OF TABLES .....	x
LIST OF EQUATIONS.....	xi
LIST OF ABBREVIATIONS .....	xii
1 Introduction.....	1
2 Literature review.....	8
2.1 The influence factors.....	8
2.1.1 The error .....	8
2.1.2 X-ray Scattering .....	9
2.1.3 Scale Calibration .....	10
2.1.4 Surface determination .....	11
2.2 Additive Manufacturing (AM) Samples.....	14
2.3 Current situation .....	18
2.4 Research gap .....	20
2.5 Conclusion .....	20
3 Methodology and Methods .....	22
3.1 Objectives .....	22
3.2 Simulation of XCT measurements .....	22
3.3 The numerical samples.....	23
3.3.1 The NIST artefact.....	23
3.3.2 The nesting spheres.....	24
3.3.3 The tube .....	25
3.3.4 Stack Cylinders .....	26
3.3.5 The stack tubes.....	27
3.3.6 The cube-cylinder AM sample.....	28
3.4 2D simulation data acquisition .....	28
3.5 3D simulation scanning.....	29
3.5.1 Nesting spheres .....	30
3.5.2 The stack tubes.....	31
3.5.3 The Cube-Cylinder AM sample .....	32
3.5.4 The tube (Figure 3-3) for investigating cone beam angles .....	33
4 Results and Discussions .....	34
4.1 2D scanning.....	34
4.1.1 The test of complex 2D samples by aRTist software .....	34
4.1.2 Stack cylinders .....	42
4.1.3 2D scan of nesting spheres.....	44
4.2 The test of 3D numerical samples.....	45
4.2.1 Nesting Spheres.....	45

4.2.2 Stack Cylinders .....	46
4.2.3 Stack tubes (open stack cylinders).....	50
4.3 AM artefacts.....	56
4.4 The effect of cone beam angles.....	62
5 Conclusion.....	67
6 References .....	69

## LIST OF FIGURES

Figure 1-1: The component of a typical XCT system [6].....	2
Figure 1-2: The workflow of complete XCT dimensional measurement [4] .....	6
Figure 2-1: The examples of additive manufacturing samples (CAD design and products): A: The test part with varying geometrical features [41]; B. Test AM artefact by Mahesh [42]; C: The test artefact built in stainless steel by DMLS [40]; D: NPL's reference sample [38]; E: The AM test part for the evaluation of angle measurement with 'book open' feature [43]; F: The testing plate for biomedical application by Teeter [29] .....	15
Figure 3-1: The NIST test artefact [46] .....	23
Figure 3-2: The nesting spheres sample .....	24
Figure 3-3 The numerical tube sample.....	25
Figure 3-4: The design and geometry features of stack cylinders .....	26
Figure 3-5: The stack tubes and specifications .....	27
Figure 3-6: The cube-cylinder AM sample.....	28
Figure 4-1: A and B. The image showing the grey value obtained under the voltages of 120kV (A) and 80kV (B). A1 and B1: The histogram of grey values within the yellow circles in image A and B respectively. A2 and B2: The plot of blue lines indicating grey value distribution within image A and B respectively.....	36
Figure 4-2: The histogram in different regions within the projection image for the voltage of 120kV.....	38
Figure 4-3: The comparison of applying scattering through the simulation XCT scanning to the NIST numerical reference sample .....	40
Figure 4-4: The comparison of mean grey value in different ladder layers (shown as attenuation thickness) within the projected image by 'non-scattered' and 'scattered' X-ray beams.....	41
Figure 4-5: 3D view of large stack cylinders and the scanned image from aRTist .....	42
Figure 4-6: The result of diameters of 2D scanning of stack cylinders .....	43
Figure 4-7: The 2D scan image of nesting sphere with aRTist at the FOD distance of 300 mm.....	44
Figure 4-8: The deviation result of the error and deviation percentages of 2D scanning of spheres .....	44
Figure 4-9: Error results for the dimensional measurement of spheres.....	45

Figure 4-10: The visualization result of XCT scanning of stack cylinders with maximum diameter of 100mm .....	46
Figure 4-11: The deviation result and deviation percentage for 100mm stack cylinders under 3D scanning and reconstruction .....	47
Figure 4-12: The visualization result of 3D simulated XCT scanning for 10mm cylinder .....	48
Figure 4-13: The error results for dimensional measurement of 10mm stack cylinders .....	49
Figure 4-14: Visualisation result for the stack tubes after simulated XCT scanning and reconstruction .....	50
Figure 4-15: The deviation results for the 3D XCT simulated scanning to open stack cylinders in two implements: without McRay scattering (thick lines) and with McRay scattering (thin lines) .....	50
Figure 4-16: The deviation results of inner and outer diameters of open stack cylinders without multi-sampling (thick line) or with multi-sampling (3×3, thin line).....	52
Figure 4-17: The deviation results of inner and outer diameters of open stack cylinders with different multi-sampling schemes (3×3, 5×5 and 30) .....	53
Figure 4-18: The deviation result for the application of multi-sampling (5x5) and McRay scattering .....	54
Figure 4-19: The comparison of the deviation results under four scanning parameters, and each of graph represents the comparison between A. no scattering no multi-sampling, scattering no multi-sampling; B. no scattering no multi-sampling, no scattering multi-sampling 3x3, no scattering multi-sampling 5x5; C. no scattering multi-sampling 5x5, scattering multi-sampling 5x5.....	55
Figure 4-20: The test sample designed by National Physical Laboratory, with positive cube and cylinder and the according negative cube and cylinder	56
Figure 4-21: A: The measurement error results for the sample in 6 scanning parameters for different geometry features based on the average of 9 measurement results; B: The deviation comparison with serious of subtraction, where N/A means the scanning parameter of non-scattered X-ray & no multi-sampling applied, and for example, '3x3 & McRay-McRay' means the data was acquired by subtracting the average deviation (Scattered X-ray only) from the deviation (3x3 multi-sampling & scattered X-ray), and yellow blocks indicate that under the row showing 'X-Y', the absolute value of deviation of condition X is lower than Y; C: Six scanning parameters indicated by numbers, which presents numbers in Figure 4-21 A and D; D: Standard deviation of the error for all 6 scanning parameters for different geometry features based on 9 individual measurements.....	59

Figure 4-22: The comparison of radius deviation against CAD model in different cone beam angles .....	64
Figure 4-23: The comparison of standard deviation value of fitting points against the fitted circle for different cone beam angles .....	64
Figure 4-24: The Ra value comparison of fitting points against the fitted circle for different cone beam angles .....	65

**LIST OF TABLES**

Table 3-1: The XCT simulation scanning settings for the acquisition of 2D projected images for NIST numerical sample, testing the influence of voltage, current and scattering contamination..... 29

Table 3-2: Scanning parameters for the nesting sphere..... 31

Table 3-3: The scanning parameter for stack tubes ..... 31

Table 3-4: Six variable scanning parameters for stack tubes ..... 32

Table 3-5: Common scanning parameters for the Cube-Cylinder AM sample . 32

Table 3-6: The variable scanning parameters of the Cube-Cylinder AM sample ..... 33

Table 3-7: Scanning parameters for the investigation of cone beam angles .... 33

Table 4-1: The comparison of deviation against fitted circle in different positions within the tube as a function of cone beam angle ..... 63

**LIST OF EQUATIONS**

Equation 1 ..... 3

Equation 2 ..... 8

Equation 3 ..... 8

Equation 4 ..... 8

Equation 5 ..... 8

## **LIST OF ABBREVIATIONS**

XCT          X-ray Computed Tomography



# 1 Introduction

X-ray computed tomography (XCT), also known as X-ray CT or CT, is a radiographic technique. XCT was first introduced by Hounsfield, the UK in 1972, and Hounsfield and Cormack from Tufts University in the USA. Both were awarded the Nobel Prize for Physiology and Medicine, for their contribution to the development of the technique [1,2]. Around the 1970s, the research began to emerge linking the use of XCT and medical purposes [3,4]. From the 1980s, the XCT has been prominent for the use of material sample investigation in non-destructive testing (NDT) purposes, including testing both inner and outer structures and identifying flaws and deficiencies within products [4,5]. The use of XCT provides an efficient detection and investigation of defects in the industry such as aviation industry and additive manufacturing.

In the field of additive manufacturing, the need for conducting a precise dimensional measurement is growing. AM samples have complex internal structures, and CMM relying on contact could not measure AM samples without destruction. Unlike CMM, X-ray computed tomography (XCT) is designed based on the attenuation of X-ray over measured samples and the completion of measurement is independent to the complexity of AM products without destroying. The advantages of X-ray computed tomography in the use of measurement includes:

- the potential in examining and measurement in non-destructive-testing (NDT);
- the ability to examine the products for both internal and external structures efficiently and simultaneously;
- the cost reduction in the process from the blueprint to the actual product.

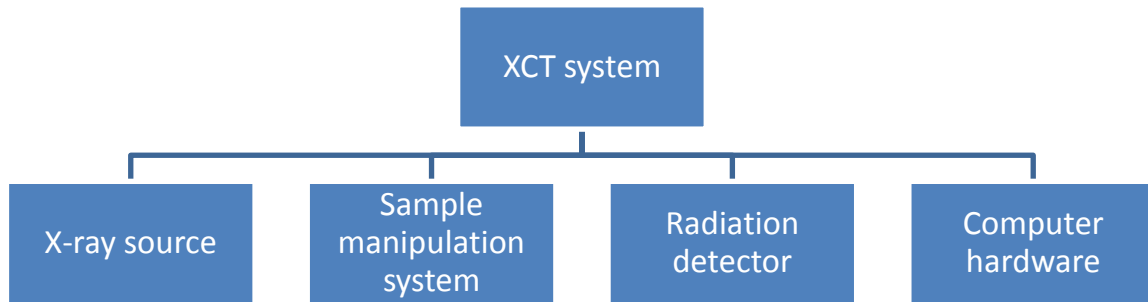


**Figure 1-1: The component of a typical XCT system [6]**

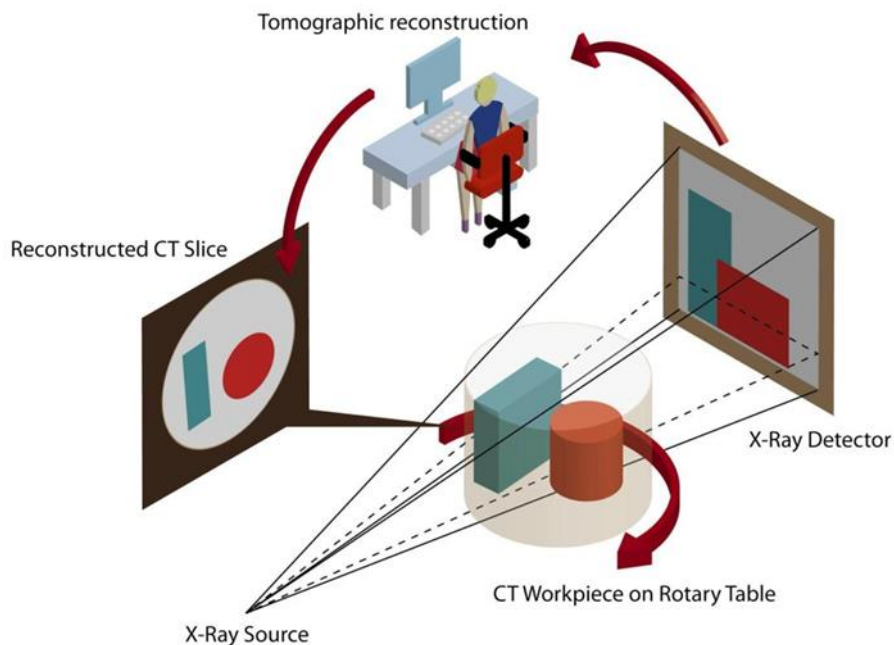


**Figure 1-2: The diagram of working principle of X-ray computed tomography [6]**

A typical XCT system has four components that include an X-ray source, a sample manipulation system, a radiation detector and a computer hardware system, as shown in Figure 1-1. Figure 1-2 presents the diagram of the workflow of the XCT scanning.

In the X-ray source, the X-ray is generated by the elevating electrons through the electric field under certain voltage impacting with the target metal material in a vacuum environment. The X-ray is emitted in two separate principles: continuous

bremsstrahlung and discrete characteristic radiation. The bremsstrahlung effect by the interaction between the negative charge electrons with the positive charge nucleus resulting in the energy loss of electrons by the form of sudden deceleration, and X-ray radiates; the characteristic radiation, however, is accomplished by the direct collide between the accelerated electrons and the shell electrons within the atom of the metal target, which causes the existence of vacancies replaced by outer shell electrons with the emitting of discrete X-ray spectrum [6]. The type of X-ray tube can be classified into directional and panoramic tubes according to the radiation direction, or be divided into unipolar and bipolar tubes, based on the arrangement of ground wire relative to the anode and cathode [6].

After the emission of the X-ray from the X-ray source, the X-ray beam penetrates the material samples with the attenuation process, whose factors have been explored in the previous study [7]. The linear attenuation coefficient was presented [8] and the equation of the intensity of the X-ray after attenuating a distance within the material can be expressed as follows [9]:

$$I(x) = I_0 e^{-\mu x}$$

Equation 1

where:

$I(x)$ : the intensity of the photon after travelling a distance of  $x$  in the attenuation

$I_0$ : the initial intensity of the photon

$\mu$ : the linear attenuation coefficient

$x$ : travel distance within the material

Several lines of evidence [10] suggest that the linear attenuation coefficient can be determined by the features of the imputed photons, like the wavelength of the X-ray, and the material properties of the attenuated substance. It is easy to find that for the X-ray beam with fixed initial intensity, the intensity of the attenuated X-ray beam after travelling a certain distance  $x$  can be calculated if the linear

attenuation coefficient is known. This equation is of great significance as it successfully provided the guideline of further reconstruction process: it gave a guidance for quantitative calculation of the X-ray intensity after attenuating the material with certain thickness, and the reconstruction can inversely calculate the thickness by knowing the initial intensity, attenuated intensity and the linear attenuation coefficient.

After the attenuation process, the attenuated X-ray illuminates the X-ray detector. There are many types of X-ray detectors in varying X-ray machines, and ISO 15708 classified X-ray detectors into two main groups: ionization detectors and scintillation detectors [6]. Different type of detectors has different working mechanisms, and for example, in direct detectors, the absorbed X-ray photons can produce electron current by producing electric-hole pairs in the bulk materials within the detector. Influencing factors of the detector includes sensitivity, field coverage, geometrical characteristics (size, pixels), quantum efficiency, spatial resolution, noise, dynamic range, uniformity, acquisition speed, frame rate and price [6].

Based on the above, from the emission of X-ray particle, to the illumination of detector, an 2D image will be obtained. Thus, the complete process of X-ray computed tomography is a cyclic process with the normal 360 degrees rotation of samples to get hundreds or thousands of 2D images, which will be transferred to the PC system for further reconstruction and data analysis.

However, the absence of international standard for XCT dimensional metrology is an inevitable issue and the accuracy, uncertainty and repeatability are still unidentified [4,6,11,12]. Without a complete international standard, it is difficult for a measurement result obtained by XCT to be properly traced, and in brief, for a measurement result acquired by following a certain illustration, other people could get a diverse result following the same instruction, as the influencing factors in XCT measurement is obscure. What is known about XCT use in dimensional metrology is largely based upon empirical studies [4,6,12,13]. The first serious discussions and analyses about XCT use as a dimensional tool emerged during the 1990s [4,14–16]. The first major milestone was presented at the exhibition in

Control Fair in Germany at the year of 2005, when the first XCT system Werth Messtechnik assigned exclusively for dimensional metrology was presented [4,17]. The main reason of the impediment of the formation of the relative international standard for XCT dimensional measurement is that the XCT is a complex system where there are variety of convoluted factors influencing the measurement results, during the whole period from the beginning XCT scanning, to the medium-stage reconstruction procedure, and to the final PC visualisation process. Much of the current literatures [12,18–22] on the XCT dimensional metrology pay particular attention to the influencing parameters onto the measurement results.

The complete measuring procedure is a combination of complex step chains. Kruth from Belgium [4] have proposed systematically the explanatory workflows during the CT dimensional measurement, including XCT measuring hardware (scale calibration, X-ray measurement process) and succedent data analysis process (raw data pre-processing, reconstruction to 3D models from 2D images, rescaling, thresholding, edge detection, voxel interpolation, geometrical determination, CMM software measurement evaluation, CAD comparison). The flow chat for accomplishing XCT dimensional measurement is illustrated in Figure 1-3.

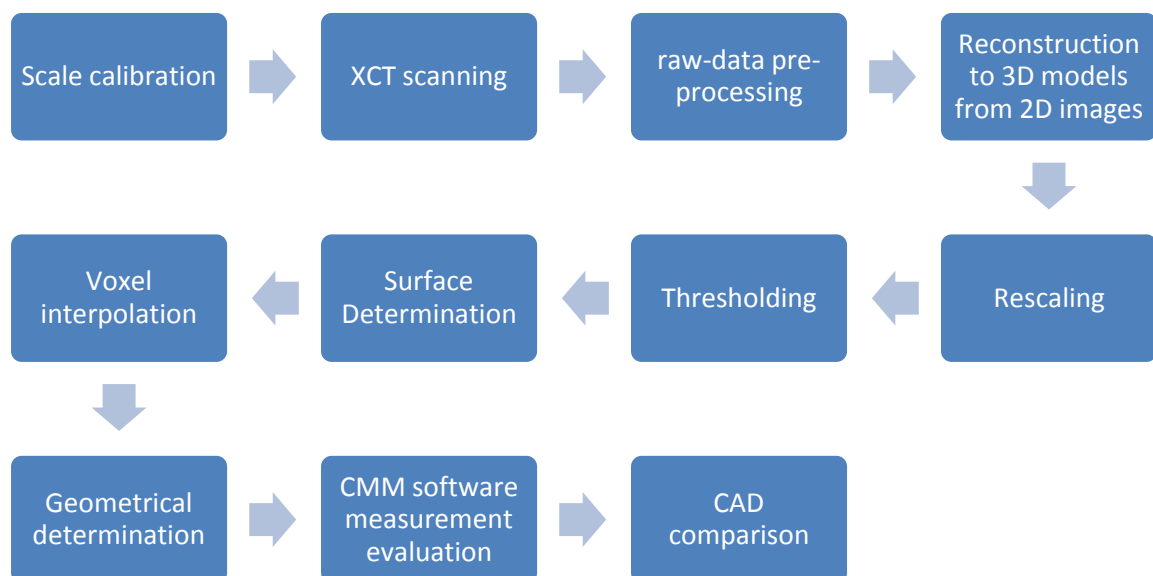


**Figure 1-3: The workflow of complete XCT dimensional measurement [4]**

Uncertain factors in each step in the measurement chain listed above might have possible impact on the outcome of measurement, and in especial, the accumulation of errors from measurement steps could cause significant deviations. The effort for the identification of potential error sources could be essential for the promotion. Some common error sources of XCT system have been understood [4,6]:

- Beam drift is primarily caused by the thermal expansion of the X-ray tube in the X-ray generation process where only 1-2% of the energy is transferred as the photon of the X-ray beam, and the remaining energy dissipation is the heat emission resulting in the increase of the temperature in the X-ray tube to distort the inner structure [6]. Dr Nadia Flay and Dr Wenjuan Sun [23] have assessed the quantitative research on focal spot drift (known as beam drift) with a novel design of a sample;
- Beam hardening is the result of the underestimation of the complexity of the emitted X-ray spectrum as typically the reconstruction process would assume the single-wavelength X-ray spectrum, which might lead to the misconception of the linear attenuation coefficient in the process of reconstruction [6]. Corcoran, H. C. [24] attempted to evaluate the impact of beam hardening on the dimensional metrology with the different orientations of the workpiece;
- Ring artefacts is caused by the incorrect alignment of the object, focal spot and the detector, and this error could lead to the sharper contrast rings of on the sample around the centre of rotation [4];
- Other error sources could include scattering, metal artefacts, noise, aliasing artefacts, sampling artefacts, filtering, rotation axis errors, adjustment errors, error from wrong identification of rotation centre, and Feldkamp errors [4].

In addition to the error sources listed above, operator preference could also influence the measurement result, however, this error source has not been

investigated. The operator can influence the measurement results by interfering with the hardware and software:

- Hardware: voltage, current, position of detector and sample (FDD=Focal spot to detector distance, FOD=focal spot to object distance), placement of the sample
- Software: surface determination by selection of voxel specimen in the raw data, geometry determination by selecting reference points on the determined surface

The 3D model is obtained by the 3D reconstruction using a large number of 2D slice images. The raw 3D model data is a combination of a mass of voxels, which is a 3D data unit with specific grey value. Thus, there are no edges or surfaces in the raw data. In order to perform dimensional metrology towards samples accurately, the surface (or namely the boundary between the material and the air) must be determined as precise as possible. Error estimation of surface can straightway affect the measurement results.

The influence of voltage and current of the electron acceleration tube [18] and the influence of position [4] has been studied and illustrated. Edge determination and subsequent geometry fitting are two essential steps during the whole measurement. The raw data with coalition of voxels with different grey values after reconstruction transfer to virtual data with surface and shapes for further measurement. Proper relative factor settings in hardware and software may help to minimise the measurement error, which shall be illustrated in the future International standard handbook.

The overall aim of this study is to develop the simulation data for the XCT soft-gauge purposes. The numerical samples with specific geometry features (cylinder, tube, sphere, cube) will be developed as the reference samples. The simulated data is used for testing the 2D slicing images and the dimensional measurement error considering scattering-contamination, multi-sampling property of the detector, voltage, sample geometry features.

## 2 Literature review

### 2.1 The influence factors

#### 2.1.1 The error

Each measurand should have the corresponding true value, however, the true value cannot be determined. Instead, the reference value (or conventional true value) is used as a high precision estimation of the true value [25]. In the measuring work, the measured value generally does not fully equal to the reference value with the influence of error sources. The absolute measurement error is defined as

$$\Delta_x = x - x_0$$

**Equation 2**

The relative error is the ratio between the absolute error and the reference value.

$$\delta_x = \frac{x - x_0}{x_0}$$

**Equation 3**

The total error could be explained by the function illustrated below

$$\varepsilon = F(\Delta_1, \Delta_2, \Delta_3, \dots, \Delta_k)$$

**Equation 4**

where  $\Delta_k$  means the error generated in each step in Figure 1-3, and

$$\Delta_k = f(x_{k1}, x_{k2}, \dots, x_{km}, y_{k1}, y_{k2}, \dots, y_{kn})$$

**Equation 5**

where  $x_{km}$  indicates the systematic error and  $y_{kn}$  presents the random error.

The error sources could be classified in systematic measurement error and random measurement error. The term ‘systematic measurement error’ refers to the error component which remains unchanged or changed in a predictable trend under repeated measurement tests. In the XCT dimensional measurement, the



systematic error includes beam hardening (caused by the characteristic of polychromatic radiation), cone-beam angle (circular trajectory of the source), scattering-contamination (direction change of rays when transmitting through inhomogeneous medium) and focal spot size. The random measurement error assumes an unpredictable trend when all predictable error sources are under the control. The correction of the systematic measurement error could be achieved by estimating the systematic error value in repeat tests, while the exact value of random error is always undiscovered due to the inability of conducting indefinite measurement tests.

### **2.1.2 X-ray Scattering**

Scattering is a phenomenon where the photon beam changes the direction when transmitting through inhomogeneous medium causing intensity change, direction deviation with an angle and (or) energy change (or wavelength change). Thus, in the real X-ray computed scanning, when X-ray beams illuminate pixels on the detector, the existence of scattering-contamination leading to multispectral, unidirectional beams is unavoidable. On that occasion, scattering-contamination could broadly influence the quality of 2D slices and further 3D models, which could make accurate dimensional measurement arduous.

In the X-ray attenuation process through the material sample, the loss of X-ray photon has two different mechanisms: photoelectric absorption and Compton scattering [4]. The photoelectric absorption occurs when the total energy of injected photons transfers to the electron in the atom to eject, while the Compton scattering is mainly due to the interaction between the incoming photons and the electrons at outer shell in the atom.

The scattered X-ray after attenuation could deviate from the original ray path and cause undesirable background on the image where the contrast could be reduced. Both the absorption and scattering are energy-dependant, thus the attenuation coefficient is not only dependent on the material and density, but also related to the energy of injected photons. However, the X-ray beam is not mono-energetic, and the dimensional measurement result can be significantly affected

when only considering the material sample in the reconstruction process relying on Equation 1 mentioned in the introduction.

Alvarez [26] summarised the mathematical method to get the equation for determining the attenuation coefficient with constants which are independent to the spectrum energy considering both photoelectric effect and Compton scattering effect. The article provides the reconstruction protocol deduction considering density-dependent scattering.

There are relatively few historical studies in the area of the influence of scattering on the XCT dimensional metrology. Lifton [27] researched the application of beam hardening and scattering to the XCT dimensional measurement result by using simulated XCT. In his work, Lifton used 5 parallel glass tubes calibrated by CMM with the calibrated data of length, inner diameter and outer diameter. After simulated scanning, the reconstruction process was conducted and surface was determined under ISO 50 and local threshold. It has been reported that under ISO 50 scheme, scattering can lower the measurement result of inner diameter and rise the result of outer diameter, while in local threshold scheme, the scattering has no significant impact on the measurement results. From this study it can be assumed that the scattering contamination could be reduced by different surface determination protocol.

### **2.1.3 Scale Calibration**

The term 'scale calibration' tends to be used to refer to the process to assign the specific value of 'pixel' in 2D slice images and 'voxel' in 3D model [4]. For the raw data, pre-processed 2D images and 3D reconstructed images, both the pixel and the voxel should be associated to the certain length units (m, cm, mm,  $\mu\text{m}$ , nm, etc.). Usually, the scale calibration' is accomplished by with a calibrated object with known geometrical features. The scale calibration can be performed before scanning, or at/after data analysis process. However, the scale calibration should be performed for the measurement setup normal operation of the XCT, which includes magnification, coordination system related to rotation axis and coordinate position of source, object and detector. The magnification is determined by the ratio of source-to-object distance (FOD) and source-to-

detector distance (FDD). Each pixel within the detector can have varying scale factor along the centre to the edge, which can cause the inconsistency when translating each voxel in the reconstructed 3D model to the specified length unit. Precise correction for the pixels calibration along X-Y plain over the detector is usually done with the installation of the detector and in such intervals. The investigation of scaling error can be converted to whether there are differences in the errors when measuring different parts of the sample.

A number of authors [28,29] have considered the effects of the position to the measurement results, however they have complete contrary findings.

Teeter [29] designed an AM artefact shown in Figure 2-1F with same shapes and sizes distributed on different positions. Once the test object was produced, the main features were measured by using a measuring microscope with the accuracy of 0.5  $\mu\text{m}$  and they were considered as the reference features. According to the measured results with XCT, the author concluded that the position did not affect the measurement results, which effectively proved that the scaling calibration process for each pixel over the X-Y plain of the detector was feasible. However, surprisingly, contrary to the above study, Hiller [28] demonstrated that in the bias assessment, compared to other parameter settings (voltage, current, prefilter thickness, etc.), the position of the section have greater impact on the measurement results. However, Tetter's research only had 1200 image slices taken while Hiller only took 720 slicing images to reconstruct 3D model. In the field of precision study of XCT dimensional metrology, there are obvious difficulties in accepting the Hiller's research conclusion by having only 720 slicing images taken.

#### **2.1.4 Surface determination**

The surface in 3D model data is determined by selecting the certain grey value. However, the surface determination is difficult because the position of the surface is determined by a chosen grey value threshold. Previous research [12,22,30] failed to explain how they conducted surface determination by simply explained 'surface determined in the software' which is not acceptable.

In dimensional measurement, the most common surface determination procedure is using the automatic ISO 50 scheme [4], in which the surface grey value is determined by selecting the middle point grey value in the histogram between the grey values representing the background and the values corresponding to the material. Some of the previous research [31,32] used the ISO 50 scheme only.

Recently researchers are focusing on the peak gradient scheme [18,24,33], which is an alternative surface determination protocol where the surface between the material and the background (or other materials) is at the point of the greatest changing rate of grey value (also named local thresholding). Kathryn [34] studied the surface determination by local threshold and measured the geometric features such as cylinder diameter, length of an insulin injection device. Kathryn concluded that instead of surface determination and geometry fitting, the definition of datum system was the main source of total uncertainty (about 11  $\mu\text{m}$  – 15  $\mu\text{m}$ ). Kraemer [32] investigated the comparison of the influence of different searching distances of 2, 4 and 8 voxels under ISO 50 scheme to the measurement results. The searching distance is defined by the region where the system searches the voxel with the greatest gradient of the grey values, and the voxel is defined as surface. Kraemer found that there were no obvious changes of deviation for different searching distances, but the application of searching distances increased the measurement accuracy compared with auto ISO 50 scheme only.

Corcoran [24] used the reference sample of aluminium hole plate produced by National Physical Laboratory to investigate beam hardening effect. The researcher set the initial threshold roughly between the background and the material as the starting threshold, and then the position with highest gradient of grey value was detected and defined as new surface. Lifton [33] and Kiekens [18] investigated both the ISO 50 scheme and local threshold scheme, however the specific local thresholding methods were different. Lifton initially smoothed the rough edge range with Gaussian filter, with the reference of Canny method [35]. He found that the local thresholding scheme was less sensitive to scattering and

beam hardening than ISO 50 scheme. Additionally, Lufton showed that the measurement deviation when using ISO 50 scheme did not exceed 60  $\mu\text{m}$ , while the local thresholding reduced the deviation to 30  $\mu\text{m}$ . Kiekens also investigated both ISO 50 and local thresholding with chrome steel spheres but he did not explain details about the local thresholding scheme. The research also showed that local thresholding can significantly reduce the deviation. The deviation was reduced from 0.142 mm to 0.014 mm (without beam hardening correlation) and from 47  $\mu\text{m}$  to 14.5  $\mu\text{m}$  (with beam hardening correlation). Lifton [27] investigated the influence of scattering and beam hardening using five calibrated glass tubes using XCT simulation scanning under both ISO 50 and local thresholding scheme in the post data processing. In this study, Lifton found that both scattering and beam hardening had influence on the measurement results in ISO 50 scheme, while under local threshold only beam hardening affected the measurement result. Townsend [36] investigated the local iterative surface determination threshold compared with ISO 50 and Otsu method for surface texture measurement, with better accuracy results, but the study did not research the local surface determination threshold method without iterative.

Besides the ISO 50 and local threshold which basically rely on grey value histogram, more innovative surface determination schemes were explored. Carmignato [37] designed fibre reference sample with holes (inner diameter) which had same diameter as the fibres (outer diameter), and found out that the deviation of outer and inner diameter had opposite trend with the increase of surface determination threshold value. Carmignato assumed that the optimum surface extraction was achieved when the deviation between the measured value and reference value for both inner diameter and outer diameter were the same. Kiekens [21] designed a reference sample with parallel grooves to measure the distances between the planes, and the researcher defined different type of the surfaces of air-to-material (AM) surface and material-to-air (MA) surface. The distance between AM and MA surface (like material thickness) could be affected by threshold value while measured distance between same type of surfaces were independent to the threshold value.

## **2.2 Additive Manufacturing (AM) Samples**

The review of AM samples could facilitate the design (geometry features, position, materials) of AM samples for multiple purposes, including for testing XCT dimensional measurement performance.

There is a large volume of published studies describing the role of AM samples in the evaluation of XCT. Current literature [29,38–40] provides some examples of AM samples used for the test of XCT system for dimensional measurement purposes, as is shown in Figure 2-1.

Figure 2-1A describes a test part used for the test of the performance of the micro-production machine. The test part comprises divergent geometry features including cubes, stack cylinders, grooves, holes, walls, etc. The researchers produced test parts by both micro-milling and additive manufacturing technique. The products were scanned by CT machines from Padova (Nikon MCT225) and Zaragoza (General Electric eXplore Locus SP cone-beam micro-CT machine). The 3D model was compared with CAD nominal value. The maximum deviation of the product geometry feature reached -6.4% for CT-Padova and 20.5% for the CT-Zaragoza. In the case of CT-Padova, the majority of the deviation percentages were less than 1%. This experiment was a good approach to show how a CT system behaves as a gauge to measure the AM part, and the researchers assumed that the measurement process by CT machine was ideally conducted. However, the XCT system could also affect significantly the measurement results, thus it was hard to isolate the error caused by AM process.

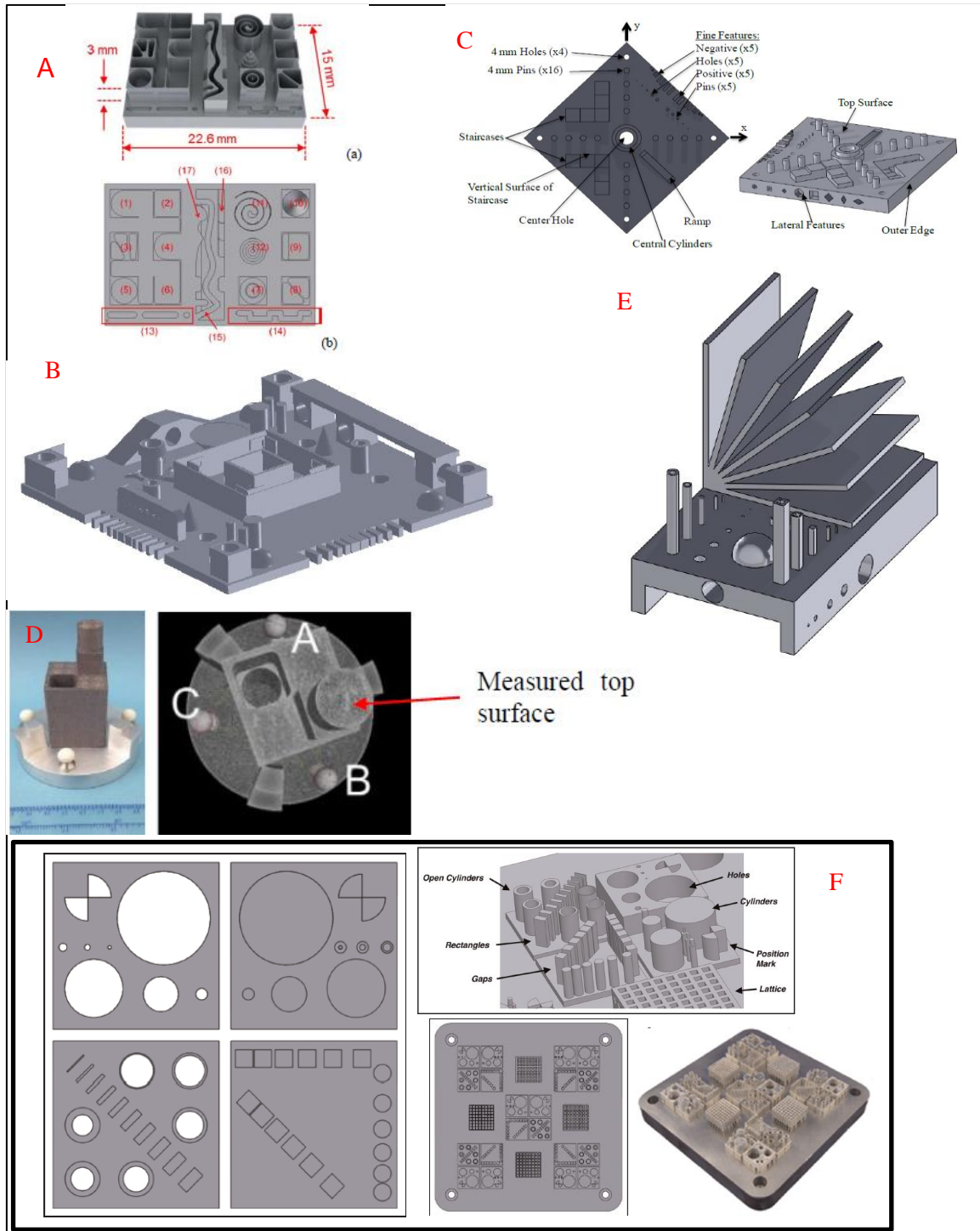


**Figure 2-1: The examples of additive manufacturing samples (CAD design and products): A: The test part with varying geometrical features [41]; B. Test AM artefact by Mahesh [42]; C: The test artefact built in stainless steel by DMLS [39]; D: NPL's reference sample [40]; E: The AM test part for the evaluation of angle measurement with 'book open' feature [43]; F: The testing plate for biomedical application by Teeter [29]**

Figure 2-1B shows a benchmark test part designed by Mahesh [42] that helped to assess the performance of various AM production machines, including SLA, SLS, FDM and LOM. The part contains a plate embedding various geometrical features including cones, cylinders, holes, bench parts, comb-shaped grooves with varying gaps, spheres, cubes walls. These geometry features have divergent dimensions, positions and orientations to ensure comprehensive testing of AM systems. The author hypothesised that the principle of designing the above geometry features is in line with existing ISO international standards (ISO 12780) to reduce further varying definition of geometry features. However, the author failed to explain the design principle in detail for each geometry part within the test plate.

Figure 2-1C shows a test part designed by Moylan [39] to test the performance of AM manufacturing systems as comprehensively as possible. The test part aimed to evaluate the AM system in distinct aspects, such as the capability to manufacture parallel and perpendicular features, circular features, fine features, etc. In contrast to Mahesh [42], Moylan explained in detail the design principle of each geometry feature, which included the macroscopic aspects such as the shape, size of the overall plate, the partial geometry design principle like the position consideration. The position decision for each geometry features were elaborately examined. The design also considered factors during the production and latter measurement, such as material, balance approach between the required volume and cost, mechanical impact among each part, feasibility of measurement using CMM and other measurement tools. What is worth to mention is that the designing criteria of the sample for the evaluation of systematic errors of AM system was considered deliberately, because the systematic errors within an AM system could be complex and difficult to identify. The author listed the systematic errors to be investigated into seven parts, including laser beam positioning, axis-positioning, alignment, beam power fluctuation, etc. The author gave detailed explanation for the function of each geometry features in the article, such as the top surface for testing the feasibility for AM system to produce flat surfaces, staircases for testing linear displacement errors, etc.



Figure 2-1D shows an NPL AM reference sample produced by the University of Birmingham [40]. The sample includes two parts: inner part and outer part. The protrude and concave parts are positioned with centre symmetry alignment and those parts have same geometry features: the cube and the cylinder. The sample was used to test the cone beam error of XCT system and laser confocal microscope. The test was conducted by measuring the top surface of protrude cylinder using both measuring system. The result showed that the measurement results from XCT had the deviation of more than 600  $\mu\text{m}$  while deviation from laser confocal microscope was around 60  $\mu\text{m}$ , which was 1/10 of the deviation from XCT system. The deviation difference implied that cone beam error of XCT system for measurement could cause significant deviation, however there are no details regarding the setting of XCT system such as the magnification index, and surface determination in the literature. In addition, more details in the XCT measurement for the AM reference sample can be researched such as the cylinder radius, distance measurement in three directions, the deviation difference for measuring inner and outer parts individually. This AM reference sample could be used as the preliminary research of XCT system for dimensional measurement purpose.

Figure 2-1E is a novel design of 'book open' structure AM sample by Castillo [43]. The sample includes multiple geometry features like 'book pages', holes with varying radius, hemisphere, tubes (cylinder and cuboid). The 'book open' part is designed for testing the capability of both the production in varying angles using AM system and angle measurement for various of measuring machines. The sample is also capable to test the AM manufacturing ability along distinct directions.

Figure 2-1F is a schematic description of the test plate designed by Teeter [29] to test the capability of production of common geometry features compatible to medical purposes by metal selective laser melting system. The basic element includes four quadrants. Each quadrant contains geometry features including walls, cylinders, gaps and holes. The geometry features within the first and second quadrants were arranged in axial symmetrical position but the first were

protrude while the second were concave. The basic element includes four quadrants. Each quadrant contains geometry features including walls, cylinders, gaps and holes. The geometry features within the first and second quadrants were arranged in axial symmetrical position. The first quadrant contained protruding features while the second quadrant was designed with pillars like structures. The basic element was replicated and positioned on four corners and on the centre of the plate so that the potential loss of production influenced by position could be tested. Four lattice features with varying gaps and wall thickness were positioned adjacent to four square edges. The measurement results showed that it was achievable to produce geometry elements with equal shapes and in different dimensions, or in different positions over the plate. Micro-CT (eXplore Vision 120; GE Healthcare, Canada) utilised the measurement of the thinnest lattice while other geometry features were measured by the measuring microscope with the accuracy of 0.5  $\mu\text{m}$ . Although the test part was primarily designed for testing the AM system production performance, the part could also potentially be used for testing the performance of x-ray system performance for dimensional measurement purposes. However, at present it is unreliable to produce a perfect AM reference sample to test the XCT measuring performance because as is mentioned in the literature, the production error for small rectangular diameter could be prominent to 194  $\mu\text{m}$  with uncertainty of 40  $\mu\text{m}$ , which was 194% of original design. The sample was also used for testing the scale calibration.

## **2.3 Current situation**

As mentioned before, when conducting XCT dimensional measurements, the complex error sources should be considered as they can largely influence the accuracy and uncertainty of the measurement results. Error sources includes beam drift, beam hardening, contamination, scattering, noises, ring artefacts, thermal expansion of the sample due to temperature change, humidity, etc.

However, some of the systematic errors could be compensated with the development of XCT systems including hardware and software. The operation temperature can be stable to minimise the influence of thermal expansion of the

sample. Beam hardening and Feldkarp artefacts can also be eliminated, and the view is supported by Kathryn et al [34] who proved that beam hardening and Feldkarp artefacts were eliminated after the process of shading correction and beam hardening correction. Also, Lifton [33] succeed in compensating the effect of beam hardening in XCT scanning.

But some systematic effects remain unavoidable. A great deal of previous research into XCT dimensional measurement has focused on the attempt of the compensation of deviations caused by focal drifts, which origins from the heat emission during the impact between the electron and the target. Nadia Flay in NPL [23] have attempted to investigate the influence of focal spot drift and the study found that focal spot drift was inevitable as well as the temperature change, which could also result in slight thermal expansion. It was difficult to eliminate the beam drift because it is caused by the thermal expansion of X-ray tube which is difficult to control. A good approach for the compensation of beam drift was presented by Probst [44]. In this study, the influence of beam drift was investigated using an in-house XCT simulation software and the compensation of focal spot drift was conducted using Matlab code, where compensation settings for the first image were also applied on the rest of slicing images, and a method for reducing the focal drift were proposed. Similarly, Frederik VOGELER [45] has been intensively investigated the influence of focal spot drift in the projection of 2D images using a calibrated plate with holes. The work explored a series of focal spot compensation experiments using balls with fixed position together with the rotated objects in the XCT machine. However, a major problem with this experiment was that the research failed to consider the latent thermal expansion of the ABS polymer socket and the steel arm connecting the stationary position balls with the machine. The coefficient of the material of balls, ABS polymer and the steel could differ and the relationship between the position of ball and the position of object could be significantly complex.

## **2.4 Research gap**

Considering these evidences, it seems that previous studies about XCT dimensional metrology were based on an assumption that the outcome of surface determination and geometry fitting were independent to the operator. However, there were no systematic experimental evidence showing that the choice of surface determination, voltage and geometry determination available to the operator in these two stages did not impact the measurement result.

## **2.5 Conclusion**

The previous section has shown that the designing principles of AM samples for test AM system purpose have been comprehensively established, and those studies outline a critical role for making a potential assumption principle for designing the AM sample for evaluating the performance of the measuring machine itself.

Overall, these studies highlight the need for investigating the performance of the XCT visualisation software as a soft gauge in dimensional measurement. The evidence presented in this section suggests that in the AM production measurement aspect, three error sources could affect the dimensional measurement results:

1. From measuring machine (hardware and software)
2. From the establishment of reference value for comparison

However, such studies remain narrow in focus dealing only with the assessment of XCT system for measurement (1) without considering the other two error sources (2 and 3) which could make the research insufficient. Taken together, in terms of the XCT dimensional measurement, these studies and the error sources listed above suggest that in order to investigate the performance of XCT system for measuring solely, it would be essential to eliminate the influence on errors from both the manufacturing process and formation of comparable reference value.

In summary, it has been shown from this review that the essential conditions for establishment of international standard for dimensional metrology using XCT in

the field of additive manufacturing are insufficient due to the lack of research over the influencing factors to the measurement. Eliminating the random errors described above in XCT research is the critical factor for the understanding of systematic factors to the measurement errors.

## **3 Methodology and Methods**

### **3.1 Objectives**

1. Design of reference artefact data
2. Simulation scanning towards different type of numerical reference samples under controlled value (multi-sampling and scattering-contamination)
3. Research the influence of scanning factors to the measurement result

### **3.2 Simulation of XCT measurements**

Use of simulation rather than actual scanning eliminates the errors sources from XCT hardware like beam hardening, beam drift, temperature change, humidity influence, contamination ring artefacts. Simulations can also control other variables, like changing voltage/current, scattering, multi-sampling. Typical XCT measurements are usually time-consuming, and simulations scanning could reduce the experimental time tremendously.

The numerical reference sample produced by software platform could include perfect geometry features like true value rather than reference value with potential errors, and when calculating the deviation further in the study, the deviation could be calculated by comparing the measured value with true reference value so that the error source from determining the reference value of samples was eliminated.

aRTist version 2.1.0 was used to conduct simulation scanning. Developed by a German company, aRTist can simulate X-ray radiation process under preferred settings in actual experimental XCT scanning, like voltage, current, filters, FDD and FOD distances, scattering, multi-sampling on detectors, detector type, pixel and sizes, materials, focal spot size, noise factors, number of slices for complete CT scanning.

This study investigated voltage, current, scattering for 2D slices. Scattering-contamination, multi-sampling and cone-beam error were researched for 3D images regarding their influence on the measurement error.

### 3.3 The numerical samples

#### 3.3.1 The NIST artefact

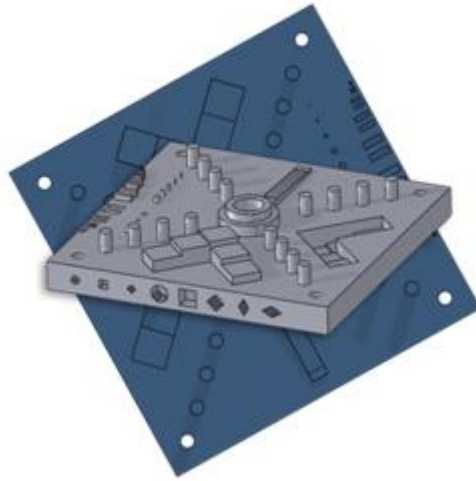
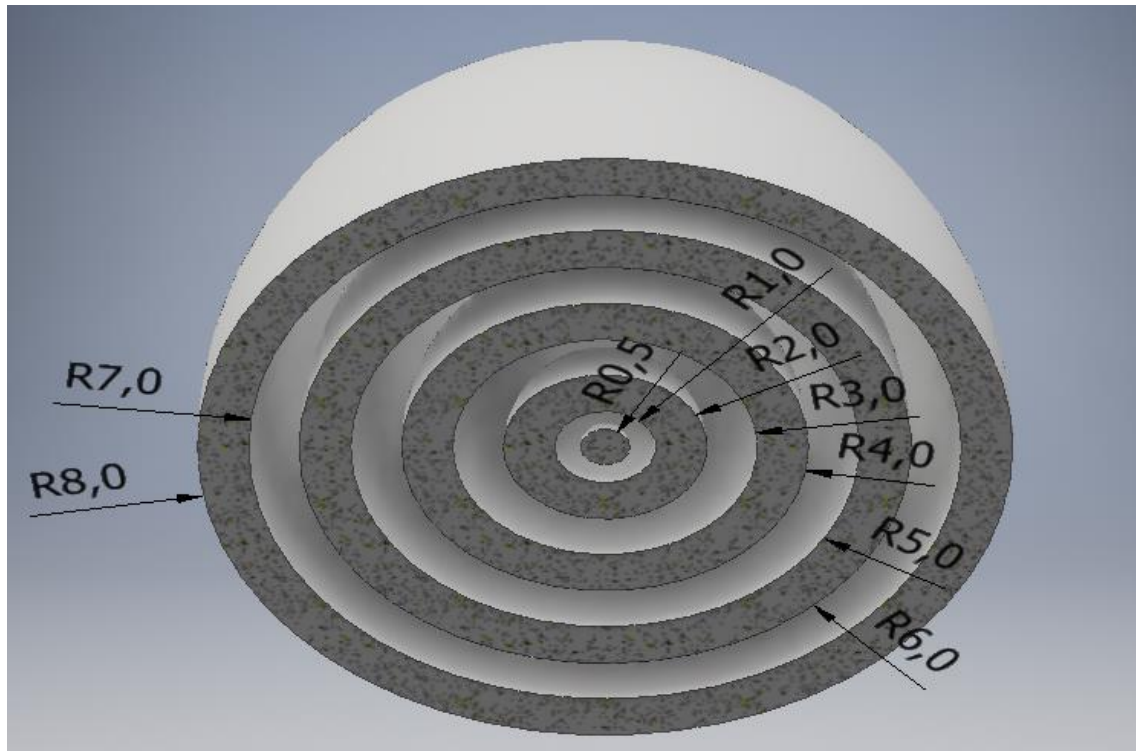


**Figure 3-1: The NIST test artefact [46]**

Figure 3-1 shows a description of an artefact designed by NIST laboratory, and this artefact is primarily used for testing the performance of AM production systems comprehensively, combining complex geometry features within the sample. STL file is available for importing into the simulation software, and the purpose of this numerical sample is to conduct initial testing of the simulation scanning software under varying settings, like voltage change, current change, multi-sampling, etc.

### 3.3.2 The nesting spheres



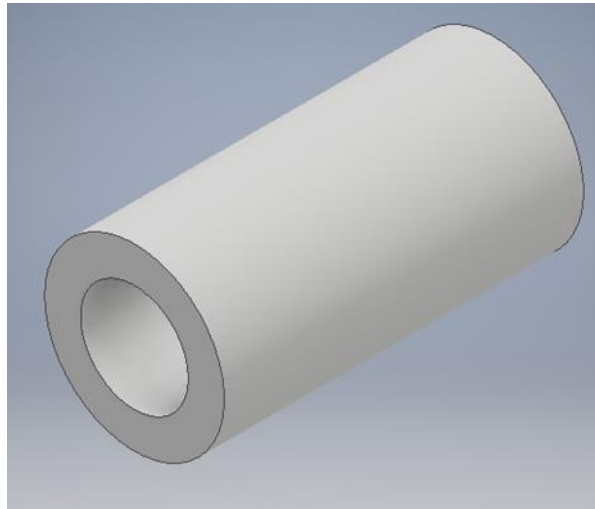
CAD model platform	Autodesk Inventor
Material	Al

**Figure 3-2: The nesting spheres sample**

Figure 3-2 presents a numerical sample consisting of nesting spheres, which was an incipient design for the measurement of spheres using XCT. This design enables one-time-scanning for the spheres with varying dimensions and types (inner and outer) of diameters, and for instance, the measurement of inner diameters is available for  $R=1$  mm, 3mm, 5 mm, 7 mm and for outer diameters  $R=0.5$  mm, 2 mm, 4 mm, 6 mm and 8 mm. The design of combining variable dimensions and diameter types could evaluate the measurement error in respect to the factor of geometry features of spheres which would be helpful for further research.



### 3.3.3 The tube

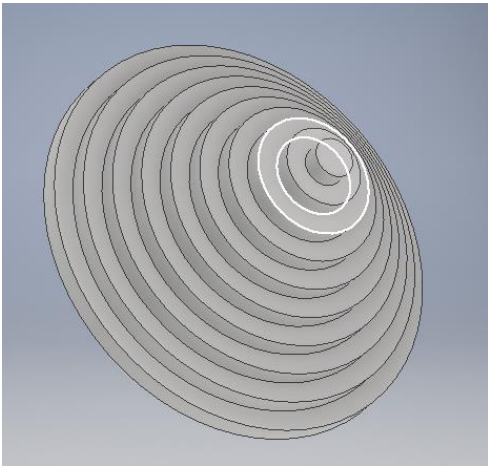


Outer diameter	10 mm
Inner diameter	6 mm
Length	20 mm
CAD model platform	Autodesk Inventor, aRTist in-built, Solidwork
Material	Al

**Figure 3-3 The numerical tube sample**

Figure 3-3 shows the tube sample designed with three different CAD platforms with specific geometry features. The numerical sample was designed for the initial test of personal influence on measurement results in different cone beam angles for the measurement of outer cylinder and inner cylinder. Meanwhile, different CAD model platforms were used to generate STL files and test the influence of CAD soft-platforms on the simulation scanning.

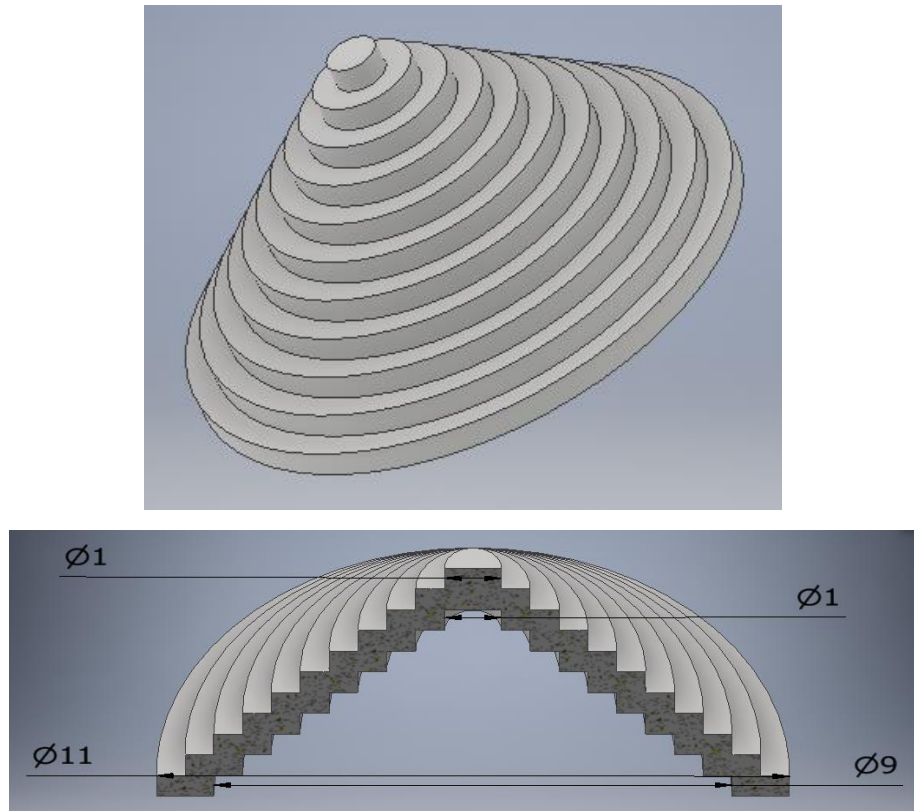
3.3.4 Stack Cylinders



Outer diameter	A: 1 mm to 11 mm
Inner diameter	1 mm to 9 mm
Height for each tube	1 mm
CAD model platform	Autodesk Inventor
Material	Al

Figure 3-4: The design and geometry features of stack cylinders

### 3.3.5 The stack tubes



Outer diameter	1 mm to 11 mm
Inner diameter	1 mm to 9 mm
Height for each tube	1 mm
CAD model platform	Autodesk Inventor
Material	Al

**Figure 3-5: The stack tubes and specifications**

Figure 3-5 describes the 3D model of numerical stack tubes sample, which is an upgrade of the tube shown in section 3.3.3. The design enables the test in varying inner and outer diameters for human factor on measurement results. In addition, the sample was used to test the influence factor of scattering and multi-sampling on measurement results in varying inner or outer diameters.

### 3.3.6 The cube-cylinder AM sample

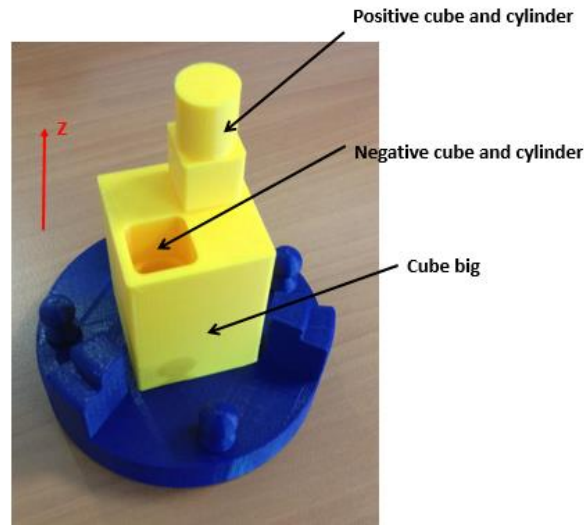


**Figure 3-6: The cube-cylinder AM sample**

Figure 3-6 shows the sample consists of positive/negative cube and cylinder with the same dimensions in centric symmetry distribution. designed by National Physical Laboratory. The sample described in Figure 3-6 was used in the following tests: the comparison of experimental and simulation data; how scattering and detector multi-sampling influenced the measurement results of diameter and side length in positive/negative geometry features; the influence of personal factors on measurement error for those geometry features.

### 3.4 2D simulation data acquisition

Prior to complete 3D scans, 2D scan offered an effective way of testing the single projected images regarding numerical test samples by simulation XCT simulation scanning. The reconstruction process analyses a stack of 2D images and converts to 3D model data, thus it has been believed that the quality of 3D model data depends on the quality of 2D projected images waiting for reconstructing to 3D model data. 2D simulation data acquisition aimed to give a preliminary evaluation of 2D projected images towards simple and complex samples in diverse simulation scanning parameters.

The basic methodology in this experimental part is comparison, with respect of different scanning parameters, and in this experiment, voltage, current and scattering were tested.

The NIST artefact (Figure 3-1), nesting spheres (Figure 3-2) were used for 2D scanning. Varying parameters were set as listed below

Settings index	Voltage (kV)	Current (mA)	Scattering
1	120	1	N/A
2	120	10	N/A
3	80	10	N/A
4	120	1	McRay 2e7 photons

**Table 3-1: The XCT simulation scanning settings for the acquisition of 2D projected images for NIST numerical sample, testing the influence of voltage, current and scattering contamination**

The variable scanning settings here included voltage, current, and scattering-contamination. Within those settings, comparison of individual scanning parameters was reliable with retaining other scanning factors same. The acquired images were imported into ImageJ and comparison and analysis were conducted.

### 3.5 3D simulation scanning

Experimental work towards data acquisition by 3D simulation scanning were performed for the investigation of scanning parameter settings, data analysis for different numerical samples. The common preparation works prior to individual studies includes:

- Numerical sample acquisition as STL file by 3D design software: Autodesk Inventor, Solidwork and in-built system (as illustrated in the numerical samples presented in Section 3.3)
- Imported the STL file into the aRTist 2.1.0 and the STL numerical data sample acted as the testing sample in XCT scanning

- Depending on the individual circumstances, scanning parameters were set in aRTist software which is presented in the following individual sections.
- The in-built program CtScan in aRTist was performed with total rotation angle of 360 degrees and 3143 total projected images, which means that the angle step size was 0.11454 degrees between two adjacent images.
- The projected images were imported into the reconstruction software (CT Pro 3D developed by Nikon XCT) and 3D raw data was generated by reconstruction after beam hardening correction (preset index 1) denoising (ramp cut off frequency 50%)
- The 3D raw data was imported into the VGStudio MAX 3.2, and local threshold edge detection was performed using 'define by selecting example area'. The term 'define by selecting example area' is the process in which the peak values of background and material in the histogram are determined by manual selection in the 3D raw data. Once the surfaces were determined, the geometry determination was addressed using Gaussian Least Square scheme by selecting reference points on the surface which would generate thousands of fitting points. Following the generation of according geometry features which comply Gaussian Least Square rule against fitting points, measurements were conducted over those geometrical shapes and comparisons of measured measurements with CAD data were implemented.

### **3.5.1 Nesting spheres**

The sample shown in Figure 3-2 were used for the complete 3D scanning for testing. It was a preliminary research over the complete measurement of spheres using simulation XCT scanning.

Voltage	120 kV	Current	1 mA
FOD	300 mm	FDD	1200 mm
Magnification	4X	Number of Slices	3143
Detector size	400mm×400mm	Detector Pixels	2000×2000
Voxel size	50 $\mu$ m		

**Table 3-2: Scanning parameters for the nesting sphere**

### 3.5.2 The stack tubes

The common settings in the simulation scanning of stack tubes were set as follows

Voltage	120 kV	Current	0.1 mA
FOD	60 mm	FDD	1200 mm
Magnification	20X	Number of Projections	3143
Detector size	400mm×400mm	Detector Pixels	2000×2000
Voxel size	10 $\mu$ m		

**Table 3-3: The scanning parameter for stack tubes**

For the stack tubes, 6 different scanning parameters were set in the following illustrations, where ‘X’ means NOT APPLIED and ‘●’ means APPLIED.

Setting index	Scattering	Multi-sampling 3×3	Multi-sampling 5×5	Multi-sampling 30
1	X	X	X	X
2	•	X	X	X
3	X	•	X	X
4	X	X	•	X
5	X	X	X	•
6	•	X	•	X

**Table 3-4: Six variable scanning parameters for stack tubes**

### 3.5.3 The Cube-Cylinder AM sample

Voltage	100 kV	Current	0.2 mA
FOD	144 mm	FDD	1200 mm
Magnification	8.33X	Number of Projections	3143
Detector size	400mm×400mm	Detector Pixels	2000×2000
Voxel size	24 $\mu$ m		

**Table 3-5: Common scanning parameters for the Cube-Cylinder AM sample**

Individual scanning parameters were set as follows:



Setting index	Scattering	Multi-sampling 3×3	Multi-sampling 5×5
1	X	X	X
2	•	X	X
3	X	•	X
4	X	X	•
5	•	•	X
6	•	X	•

**Table 3-6: The variable scanning parameters of the Cube-Cylinder AM sample**

#### **3.5.4 The tube (Figure 3-3) for investigating cone beam angles**

Voltage	100 kV	Current	0.2 mA
FOD	80 mm	FDD	1200 mm
Magnification	15X	Number of Projections	3143
Detector size	400mm×400mm	Detector Pixels	2000×2000
Voxel size	13.333 $\mu$ m	Scattering	N/A
Multi-sampling	3x3	Fitting points	3001

**Table 3-7: Scanning parameters for the investigation of cone beam angles**

The numerical tube sample was scanned under the conditions listed in Table 3-7. In the geometry determination step, circles were selected in different position of the tube, with according X-ray cone beam angles.

## **4 Results and Discussions**

### **4.1 2D scanning**

#### **4.1.1 The test of complex 2D samples by aRTist software**

##### **4.1.1.1 Voltage**

After the position of the detector, sample and the source were fitted, two single scanning was performed under the voltage of 120kV and 80kV respectively while other parameters remained the same. The exposure time was automatically calculated when the maximum grey value was set to 60000.

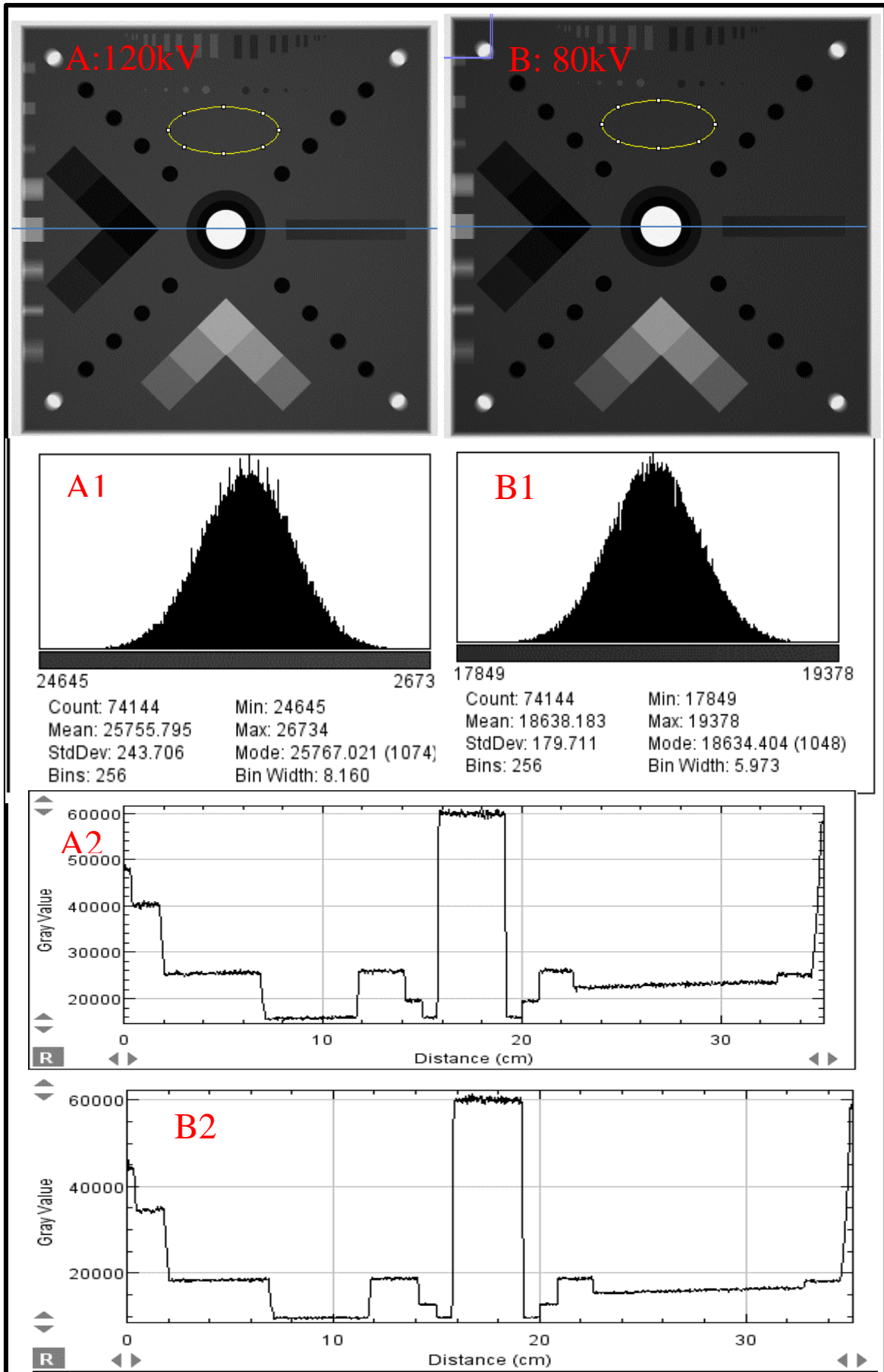


**Figure 4-1: A and B. The image showing the grey value obtained under the voltages of 120kV (A) and 80kV (B). A1 and B1: The histogram of grey values within the yellow circles in image A and B respectively. A2 and B2: The plot of blue lines indicating grey value distribution within image A and B respectively.**

In XCT machine, increasing the voltage can effectively decrease the wavelength of emitted X-ray and thus increase the intensity of X-ray illuminating the pixels of the detectors after attenuation through the sample.

Figure 4-1 A and B provide the simulated greyscale images showing the intensity of X-rays after passing through the object under the voltages of 120kV and 80kV, respectively. A1 and B1 are the grey value histograms within the yellow circle zones in image A and B. In A2 and B2 the grey values are plotted across the horizontal centre line (blue lines) in image A and B.

As expected, in A1 and B1 the mean grey value was 25756 under 120kV while it was only 18638 under 80kV, which indicates that the intensity of X-ray under 120kV illuminating the detector was greater than under 80kV after attenuation through the material.

Figure I: The grey value histogram for varying regions

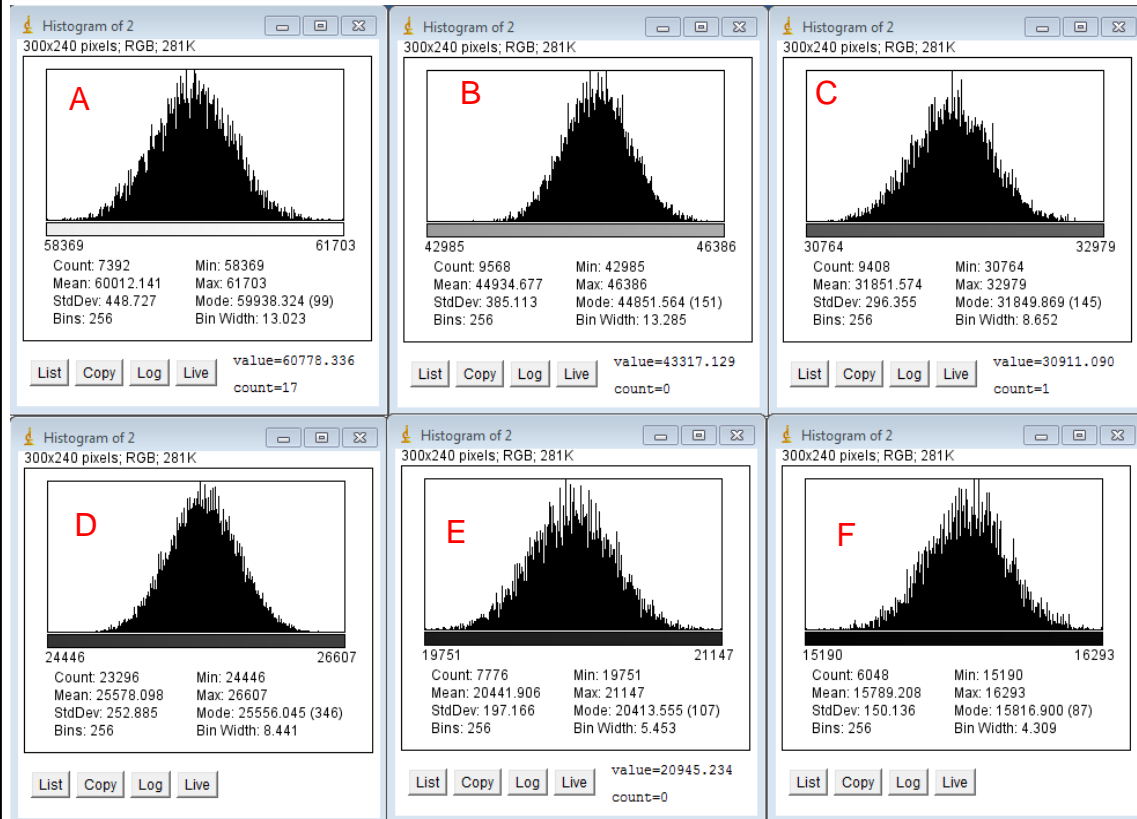
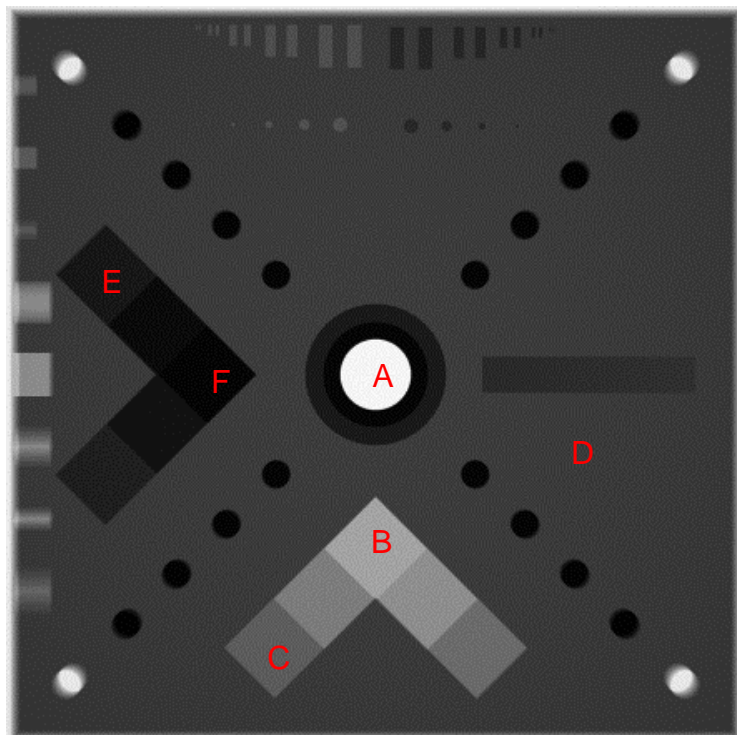


Figure II: The 2D slice image under the voltage of 120KV with alphabet labels



**Figure 4-2: The histogram in different regions within the slice image for the voltage of 120kV.**

Surprisingly, a further issue that emerged from A1 and B1 was that the standard deviation of grey values in higher voltage was more significant than in lower voltage. It could be believed that the value of standard deviations could reflect the degree of noise. Thus, it could be found that X-ray projection with greater voltage acceleration generated more noises than X-ray with lower voltage acceleration. Figure 4-2 provides the histogram results obtained by selecting different regions within the NIST sample projection image under the voltage of 120 kV. In Figure 4-2 there is a clear trend of decreasing standard deviations for thicker penetration. To be specific, the region with void penetration (area A) could see the most considerable grey value standard deviation of 448.727, while the darkest area (thickest part, area F) had shown the least standard deviation of 150.136. Hence, it could conceivably be hypothesised that the emitted X-ray was not the mono-spectrum, but the spectrum with multiple wavelengths. The X-ray generated by greater voltage could bear more multiple wavelength particles with more fluctuated intensity, which could generate maximum noises on the detector as shown in Region A. Differences of the sample thickness, or in other words, the attenuation travel distance, might have influenced the constitution of the X-ray spectrum, where X-ray with specific frequencies might have been entirely absorbed, which formed a trend to mono-spectrum. The more attenuation distance that the X-ray travelled, more absorption occurred, and more trend to mono-spectrum and mono-intensity, and fewer noises generated onto the detector.

According to A2 and B2, because of the set of maximum grey values of 60000, the grey values at the centre were similar when the X-ray particles transported from X-ray source to the detector through the centre hole without attenuation through bulk material. One of the most notable differences between 120kV and 800kV group is that the time recorded was 12.27s for 120kV and 37.81s for 80kV. For the grey values indicating attenuation through materials, as shown in A2 and B2, it is obvious to observe that the 120kV group reported significantly more grey value than the 80kV group. The time difference indicated that the detector needs

more exposure time to reach the same maximum value of 60000 under 80 kV without the material. This result may be explained by the fact that due to the smaller amount of intensity of X-ray under 80kV, in order to reach the same grey value raised from direct illumination, more time should be used. Besides, a possible explanation for the inconsistency of grey values under 80kV and 120kV may be the lack of adequate intensity to attenuate through the material. There was a fewer possibility for X-ray with lower energy (80kV group) to penetrate through the material compared with 120kV group generating X-ray with the shorter wavelength.

To sum, the higher voltage could have boosted the ability of attenuation and increased the chance for reaching the detector, but higher voltage also could have generated extra noises on the projected images, which could decrease the quality of the image and thus affect the error of further measurement.

#### **4.1.1.2 Current**

The current can effectively increase the intensity of X-ray without changing the spectrum features. To be specific, the wavelength feature and the frequency feature are stable when changing the current only. It was expected that the proportions between two grey values chosen randomly from two different X-ray beams reaching detector pixels after the attenuation through two same material parts with different thickness would not change. Two sets of experiment were conducted under the same voltage of 120kV, and under the current of 1mA and 10mA respectively. The result showed that no apparent differences were found for the two images in the different current, but the exposure time was 123s and 12.3s under the current of 1 mA and 10 mA respectively. A possible explanation is that without changing the acceleration voltage which primarily determines the energy of X-ray beams, the current value represents the number of photons penetrating the region of unit area per second. As tenfold current applied, the region with same area was permeated by tenfold photons per second, and the time for the illumination against pixels on the detector to reach the same grey value in 2D slices was reduced by ten times.

#### 4.1.1.3 Scattering

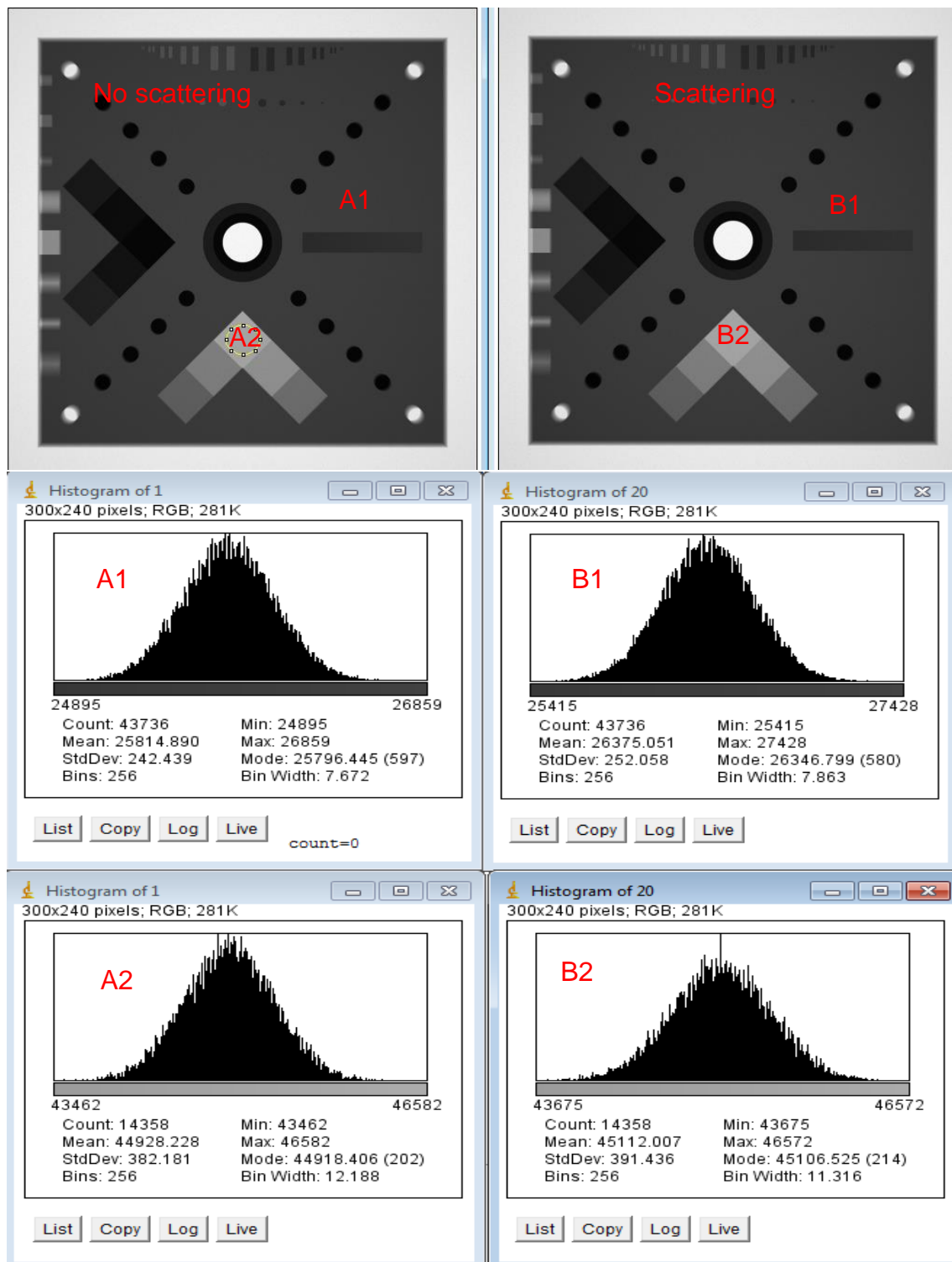


Figure 4-3: The comparison of applying scattering through the simulation XCT scanning to the NIST numerical reference sample



Figure 4-3 compares the histogram results obtained from XCT simulation scanning under the conditions of ‘no scattering’ and ‘scattering’ by selecting two individual zones within each image. ‘Scattering’ projection is different from ‘non-scattering’ in a few respects. Firstly, there is a slight increase of the standard deviation for the ‘scattered’ image compared with the ‘non-scattered’ image, with the average increase of 10 unit in the grey value in standard deviation. The reason could be attributed to the fact that the scattered X-ray after the penetration process might lead to more dispersion of the intensity which would be reflected from the detector.



**Figure 4-4: The comparison of mean grey value in different ladder layers (shown as attenuation thickness) within the projected image by ‘non-scattered’ and ‘scattered’ X-ray beams.**

Secondly, there were also differences in the mean grey value when comparing the same regions for ‘scattering’ and ‘non-scattering’ X-ray beams. Figure 4-4 compares the summary statistics for the mean grey value differences for varying attenuation thickness by non-scattered and scattered X-ray beams. What stands out in this figure is the steady growth of mean grey value differences when the

attenuated material became thicker. In general, the grey value of projection by scattered X-ray was higher than non-scattered X-ray, which could be illustrated by 0 mm thickness in Figure 4-4, where there is an only 13.33 increase of the grey value for scattered X-ray. What is interesting in this figure is the continual growth of the differences (calculated by scattered mean value subtracts non-scattered mean value) with the increase of thickness, and the difference is likely to show a steady increasing trend for the thickness over 17mm. This result indicates that for 2D slices, the influence level of scattering-contaminated X-ray beam could be largely related to the attenuation distance.

#### 4.1.2 Stack cylinders

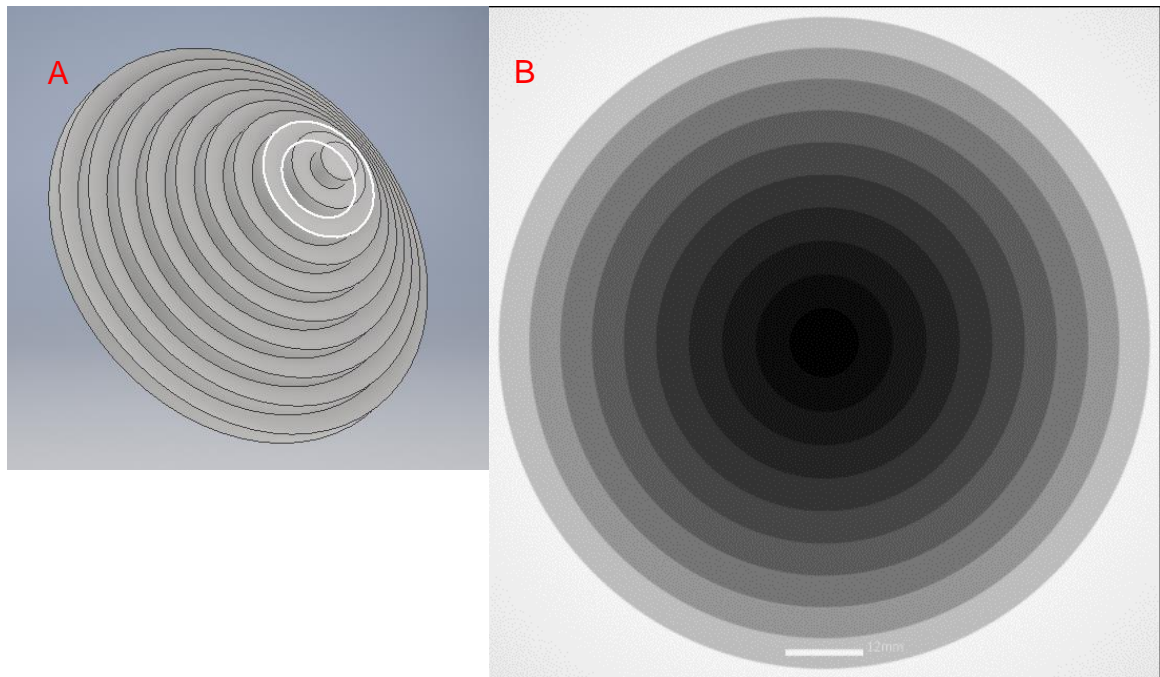


**Figure 4-5: 3D view of large stack cylinders and the scanned image from aRTist**

Figure 4-5A shows the 3D view of 10 stack cylinders with diameters from 100 mm to 10 mm with 10 mm intervals, and each cylinder has the thickness of 10 mm. The design philosophy of stack cylinders is that researcher can use this reference

sample to test factors related to varying sizes simultaneously. Figure 4-5B shows the 2D scanning image got from aRTist software.

The image was imported into ImageJ software, and the dimensional scale was set according to the datum line indicating 12mm in Figure 4-5B. The diameters were measured by the selection of each circle after choosing different threshold grey values. Finally, the diameters were calculated by measured area values for each selected circle.

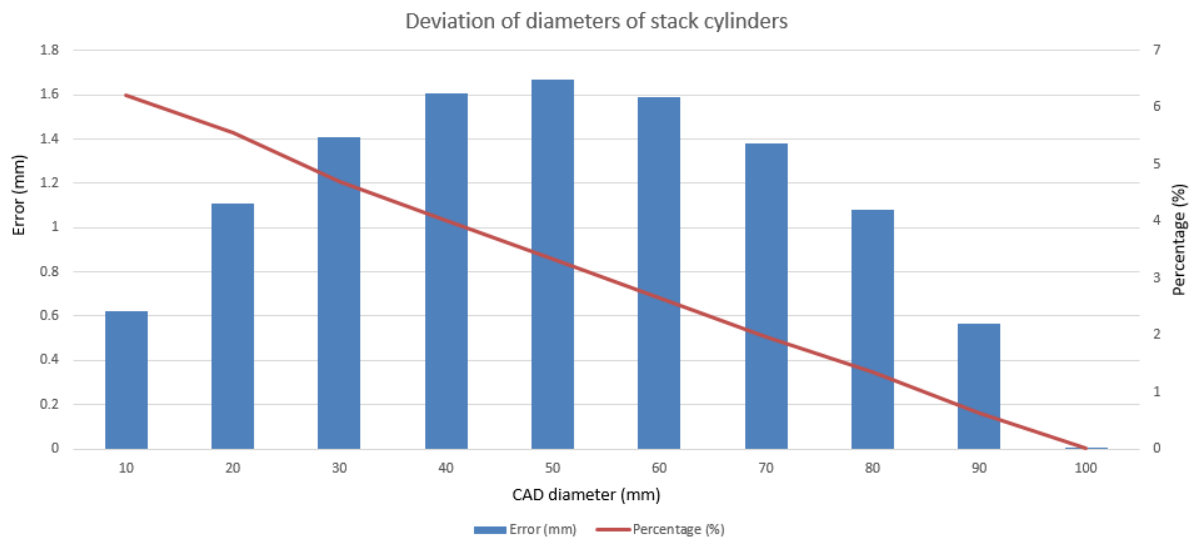


**Figure 4-6: The result of diameters of 2D scanning of stack cylinders**

Figure 4-6 describes the error of measured diameter against the CAD design data and the deviation percentage. It is worth highlighting that the trend of deviation percentage appears linear distribution, from 6.2% at  $\Phi=10\text{mm}$  to 0.0074% at  $\Phi=100\text{mm}$ . The maximum deviation was 1.67mm at the diameter of 50mm, and the trend of deviation goes up from 10 to 50 mm and decreases from 50 mm to 100 mm.

4.1.3 2D scan of nesting spheres

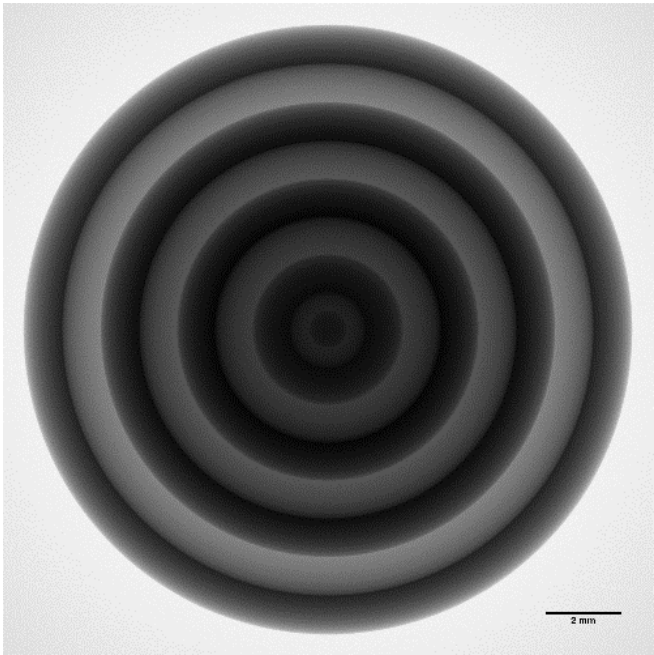


Figure 4-7: The 2D scan image of nesting sphere with aRTist at the FOD distance of 300 mm.

The 2D tests were performed within aRTist software under two controlling parameters: FOD distances of 900mm and 300mm respectively.

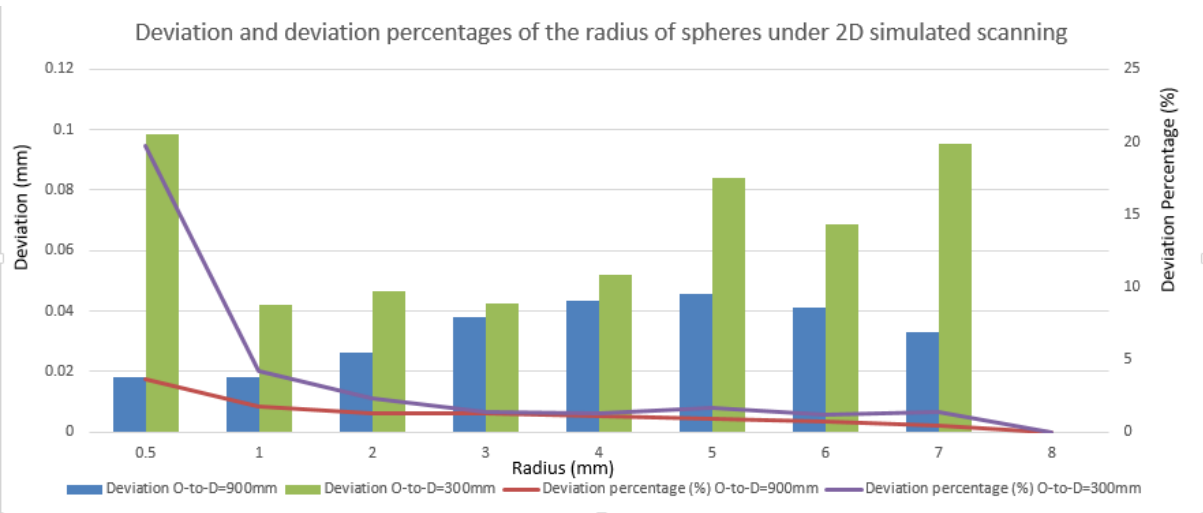
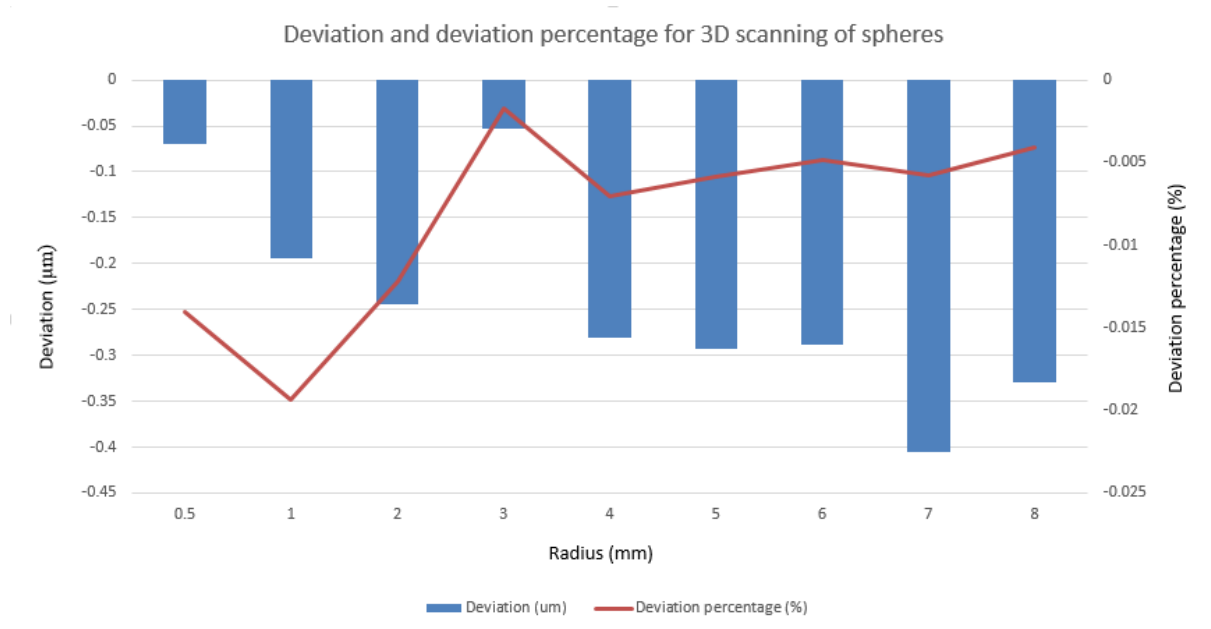


Figure 4-8: The deviation result of the error and deviation percentages of 2D scanning of spheres

Figure 4-8 describes the errors and error percentages of 2D scanning images of the sphere sample in two O-to-D distances. The reason why deviations at the radius of 8mm were 0 was that the 8mm sphere was set as the standard scale. According to the cone beam error for in the XCT scanning, it was assumed that the deviation would decrease with more FOD distance. However, on the contrary, the deviations for FOD distance of 300 mm was less than for FOD distance of 900 mm.

## 4.2 The test of 3D numerical samples

### 4.2.1 Nesting Spheres



**Figure 4-9: Error results for the dimensional measurement of spheres**

Figure 4-9 illustrates the measured error compared with CAD model design data. Surfaces were determined based on the local threshold scheme. A significant improvement was achieved compared with the error results under 2D scanning which was described in Figure 4-8. Compared with the minimum deviation of 18μm in the 2D scanning of spheres, the maximum error was only -0.41μm. Similar to 2D scans, the deviation percentages show lower for spheres with a higher radius. However, all deviations compared with the CAD model had the

negative sign, which means that the measured values are smaller than CAD reference value.

## **4.2.2 Stack Cylinders**

### **4.2.2.1 Large cylinders**

The shape of the sample described in this experiment is shown in Figure 4-5, with the maximum CAD design diameter of 100mm. The voltage and current of the tube were set as 120kV and 1mA.

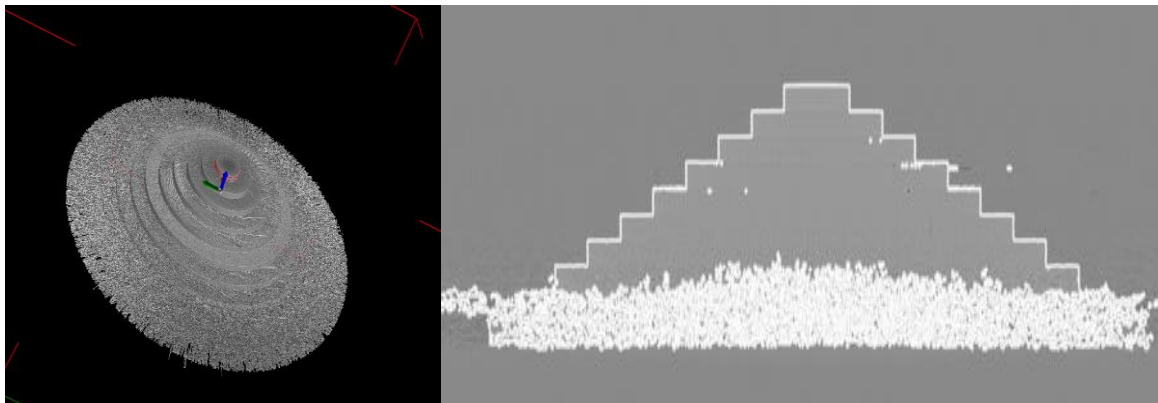


**Figure 4-10: The visualization result of XCT scanning of stack cylinders with maximum diameter of 100mm**

The two images in Figure 4-10 describe the 3D visualisation after simulation XCT scanning and reconstruction process towards the 100mm stack cylinders in the oblique view and x-z plain view respectively. It is obvious to find that noises arose within the cylinders with the diameters above 80mm, thus finding the surface of the 90mm cylinder could be troublesome. This result could suggest that 80mm of thickness could be a limit for the traversing of the X-ray beams with 120kV voltage and 1mA current. Above 80 mm of thickness, lack of data could emerge resulting vast noises.

According to the 2D scanning results illustrated in Figure 4-2, the standard deviation for the grey value in the 2D image showed a decreasing trend with rising X-ray attenuation distance. However, based on the experimental fact of the vast noises in the cylinders above 80 mm diameter, a possible explanation for this

might be that the 'noise' in reconstructed model data is not the reflection of 'noise' in 2D images. '2D noise' was generated by the fluctuation of grey values or the fluctuation of X-ray intensities illuminating the detector (and after attenuation). Considering the default set of noise removal in 3D reconstruction, the '3D noise' might be the result of improper noise removal process for some fractions in 2D images which had a less standard deviation in grey value (or less noising). The result of noise removal resulted in over noise reduction for thick parts which generated '3D noise' in the 3D model. It is possible, therefore, that noise removal should not be unquestioningly conducted in 3D reconstruction for thick parts, where reached 80 mm in this study.

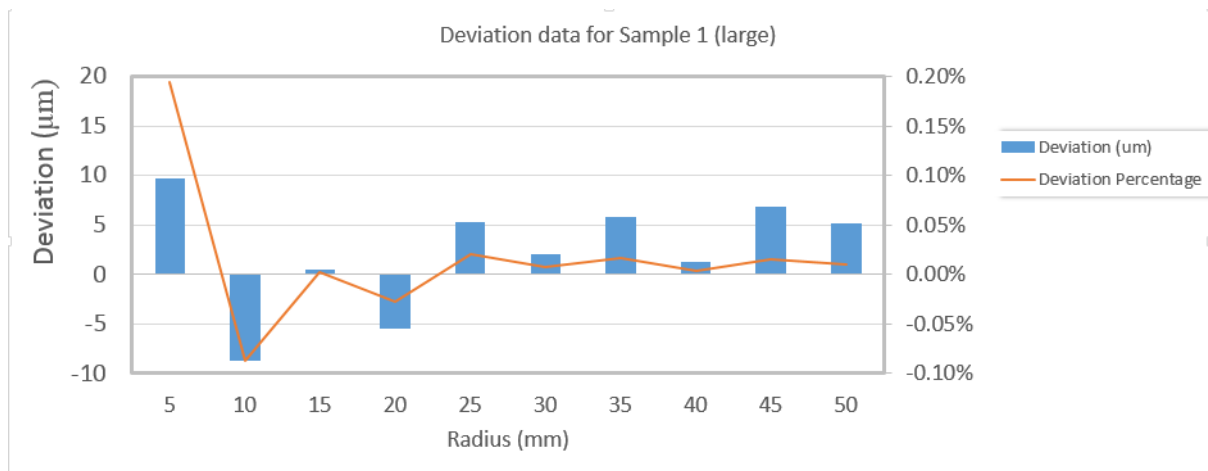


**Figure 4-11: The deviation result and deviation percentage for 100mm stack cylinders under 3D scanning and reconstruction**

The result of measurement errors and error percentage for the 100 mm stack cylinders are illustrated in Figure 4-11. In general, compared with the measurement results under 2D scan, 3D scanning shows considerable improvement in accuracy, where maximum deviation was  $9.5\mu\text{m}$  for the smallest cylinder with the diameter of 10mm. However, two of the results show the negative value, indicating that the measured value was less than the CAD design data. Furthermore, unlike the stable trend of the deviation percentage for 2D scanning, there are fluctuations in the deviation percentage under 3D XCT scanning.

#### 4.2.2.2 Small stack cylinders

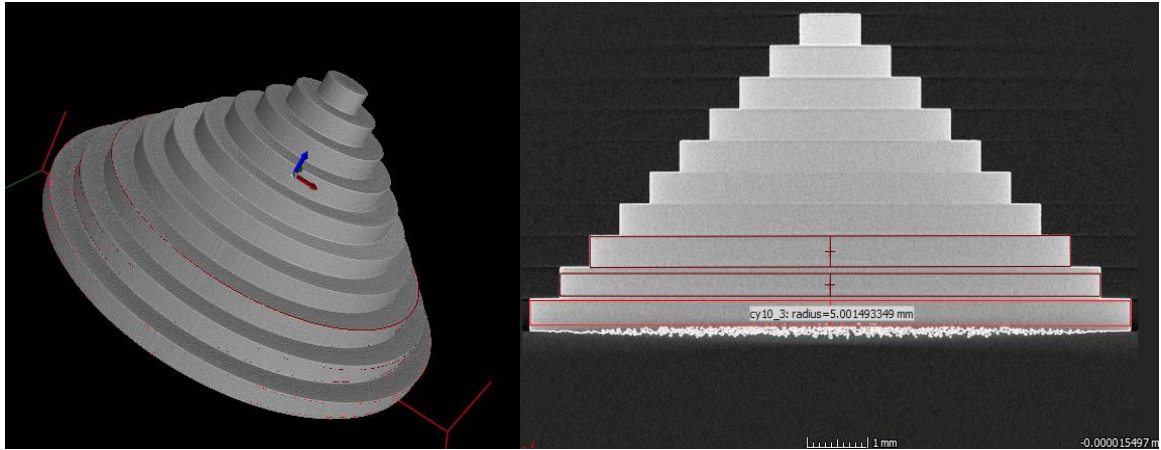


**Figure 4-12: The visualization result of 3D simulated XCT scanning for 10mm cylinder**

The maximum diameter of small stack cylinders was 10mm, with the same shape as described in Figure 4-5. Figure 4-12 shows the visualisation of the 3D simulation XCT scanning towards 10mm stack cylinders. While there are still noises at the bottom of 10mm cylinder, it is significantly evident to observe the surface of the material compared with specific cylinders above 80 mm within the 100 mm stack cylinders. Hence, it could conceivably be hypothesised that reduced attenuation distance could decrease the volume of noise voxels in the 3D reconstructed module.



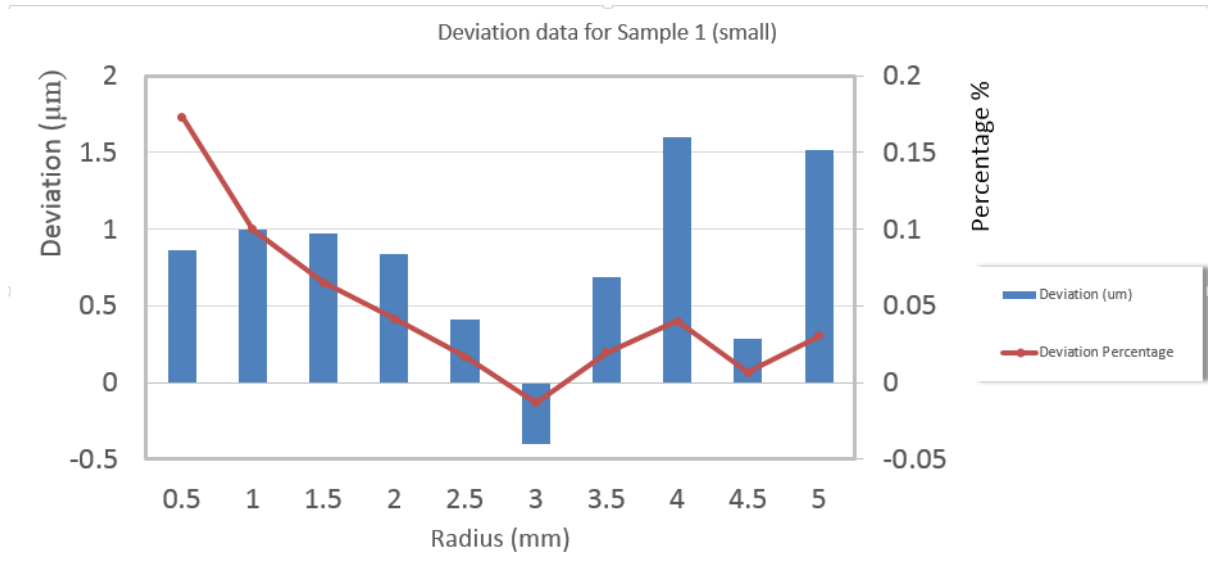


**Figure 4-13: The error results for dimensional measurement of 10mm stack cylinders**

Figure 4-13 presents the dimensional measurement errors for the radius of each cylinder within 10 mm stack cylinders. There was a vast improvement in reducing the deviation from 9.5  $\mu\text{m}$  at the diameter of 10 mm in 100 mm stack cylinders to 1.6  $\mu\text{m}$  at the diameter of 8 mm in 10 mm stack cylinders. Except for the radius of 4 and 5 mm cylinders, other measurement errors for other cylinders were less than 1  $\mu\text{m}$ . It is clear to observe that the overall size of the sample had an enormous impact on the measurement error. Besides, most of the deviations have the positive value, indicating that measured value by XCT was larger than origin CAD design values, except for the data from the cylinder with the radius of 3 mm, whose measured diameter error was -0.15  $\mu\text{m}$ . The measurement error shown here is basically random. It can be hypothesised that the errors are the result of combined influence of the spatial position and the X-ray penetration distance.

### 4.2.3 Stack tubes (open stack cylinders)

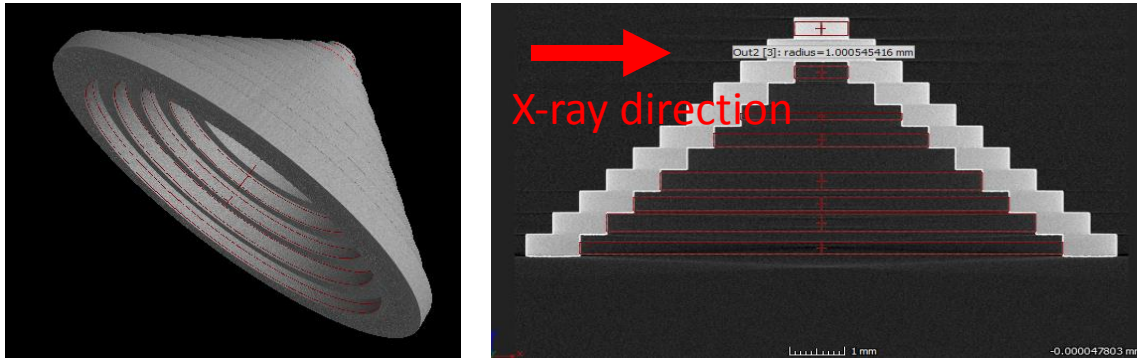


**Figure 4-14: Visualisation result for the stack tubes after simulated XCT scanning and reconstruction**

Figure 4-14 shows the visualisation models in 3D view and x-z plane view for open stack cylinders. Compared with the visualisation results for large and small cylinders described in Figure 4-10 and Figure 4-12, the visualisation results for open stack cylinders is positive considering noise level. Primarily decreased noises eased the detection of surfaces resulting from a shorter distance for X-ray beams to attenuate the material.

#### 4.2.3.1 With and without McRay scattered X-ray [33]

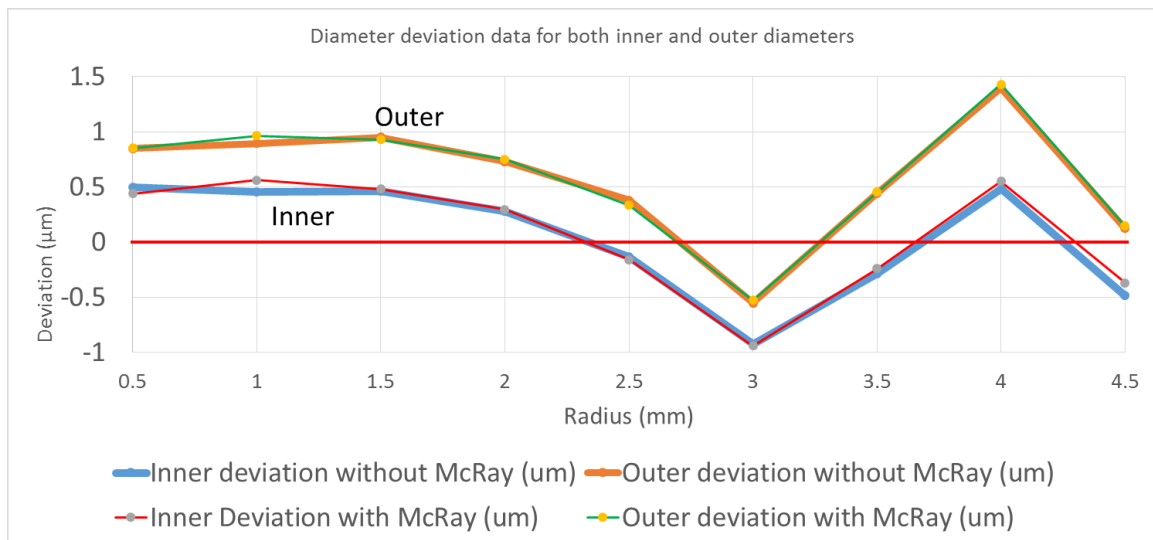


**Figure 4-15: The deviation results for the 3D XCT simulated scanning to open stack cylinders in two implements: without McRay scattering (thick lines) and with McRay scattering (thin lines)**

Figure 4-15 describes the measurement deviation of inner and outer diameters for the open stack cylinders attenuated by non-scattered and scattered X-ray. What is striking is that measurement errors for both inner and outer diameters show the similar trends. As shown in Figure 4-15, all four lines show smooth curves for radius from 0.5 mm to 3 mm, then a sharp increase to the radius of 4 mm, and finally decrease to 5 mm radius.

The implement of McRay scattering had no noticeable impact on the measurement results, except for the inner and outer radius of 1mm, where the scattered X-ray produced an increase of 0.1  $\mu\text{m}$ , which is 1/100 of the voxel size. By the present results, the previous study by Lifton (2017) [27] have demonstrated that the X-ray scattering contamination had no significant impact on the measurement result for inner and outer cylinders under the local threshold surface determination scheme, and the changes resulting from scattered X-ray was 1/20 of the voxel size. This study was successful as the corroborated the conclusion summarised by Lifton, with a vast improvement from 1/20 of Lifton research to 1/100 in this study. This data and discussion suggest that though scattering contamination is inevitable when producing X-ray, scattering contaminated X-ray would be a minute or negligible factor influencing the future X-ray dimensional measurement.

#### 4.2.3.2 With Multi Sampling only

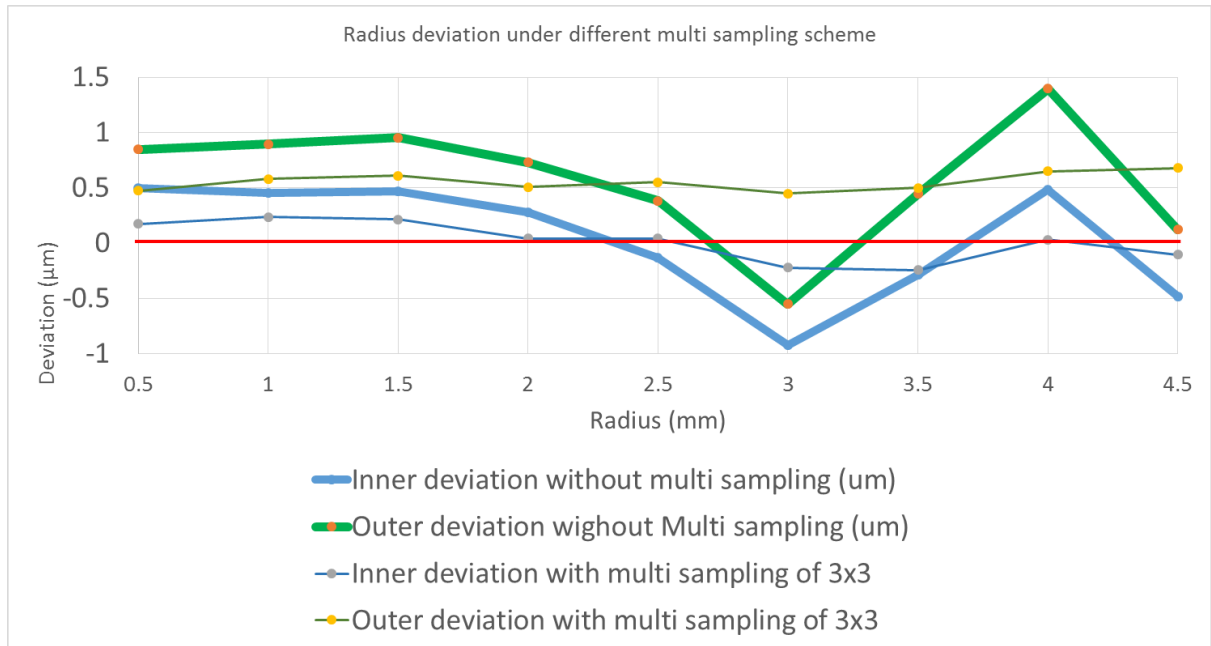


**Figure 4-16: The deviation results of inner and outer diameters of open stack cylinders without multi-sampling (thick line) or with multi-sampling (3x3, thin line)**

There are no previous work concerning the multi-sampling. Figure 4-16 presents the measurement errors of the inner and outer diameters of open stack cylinders with or without multi-sampling. A positive finding is that the implement of multi-sampling could significantly increase the measurement accuracy compared with no settings of multi-sampling. The measurement error for inner diameters of cylinders with the radius of 2mm and 2.5mm had reduced remarkably to  $0.05\mu\text{m}$ , compared with  $0.25\mu\text{m}$  and  $0.2\mu\text{m}$  with no multi-sampling settings. The error decrease might ascribe the improvement of 2D slices by means of 3X3 multi-sampling. However, for outer diameters, the result indicated that the measurement error was generally higher than inner diameter measurement errors.

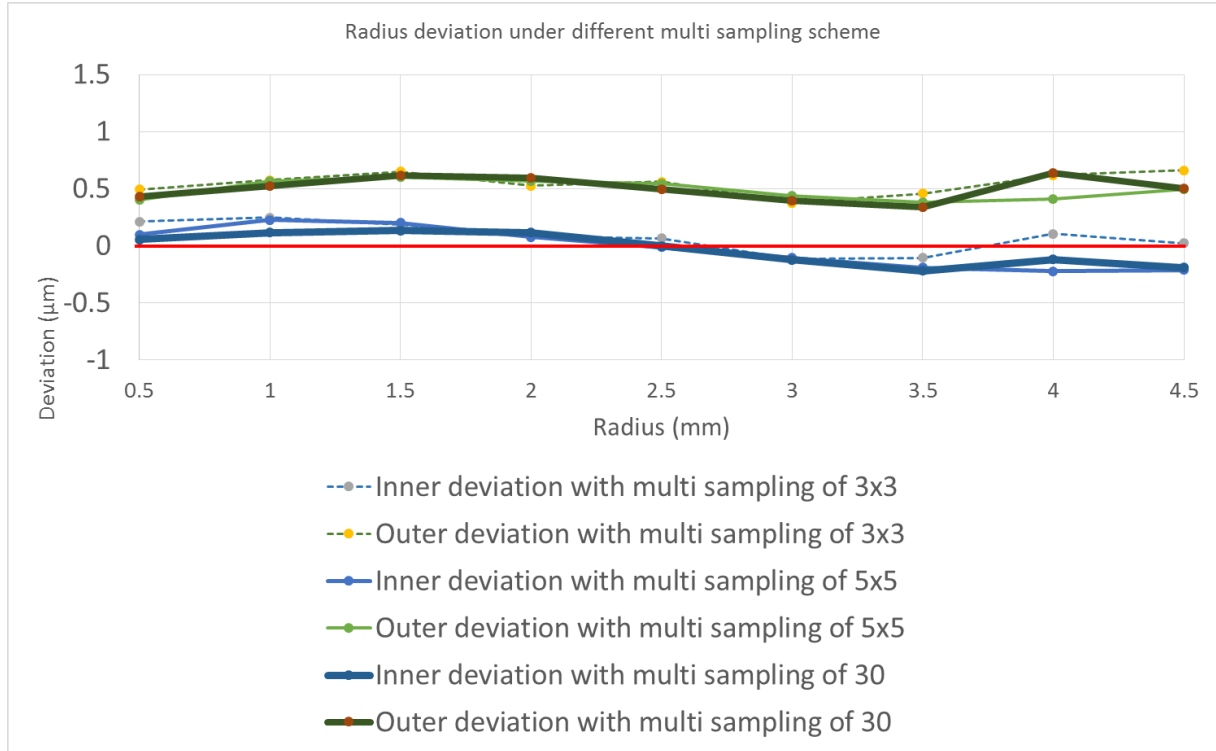


**Figure 4-17: The deviation results of inner and outer diameters of open stack cylinders with different multi-sampling schemes (3×3, 5×5 and 30)**

Figure 4-17 illustrates the measurement errors for inner and outer diameters of open stack cylinders with varying multi-sampling schemes. Although the implication of multi-sampling could increase the accuracy compared with no multi-sampling settings, further increase of multi-sampling value has no impact on the accuracy of measurement, and the trends were irregular as a function of multi-sampling value.

#### **4.2.3.3 With Multi Sampling (5×5) and McRay scattering simultaneously**

Figure 4-18 describes the deviation results for measuring the radius of inner and outer cylinders under four parameter settings: without either multi-sampling or McRay scattering, multi-sampling (5x5) only; McRay scattering only; multi-sampling (5x5) and McRay scattering simultaneously.

The pixel size was 10μm×10μm, (voxel size of 10μm×10μm×10μm), and the maximum deviation was around 1.45 μm in measuring the outer diameter of the 4 mm radius with the condition of considering McRay, and the maximum deviation was about 14.5% of the pixel size. However, except for the measurement result

to 4mm radius outer diameter, all other measurement results were below 1  $\mu\text{m}$ , with the maximum deviation of 0.965  $\mu\text{m}$  (9.65% of pixel size). Regarding the outer radius, under the parameter setting of multi-sampling only, there was no visible fluctuation for the deviation, and the mean value of deviation was approximately 0.5  $\mu\text{m}$ ; The application of McRay increased the magnitude of fluctuation, but the mean deviation value was also approximately 0.5  $\mu\text{m}$ . It is interesting to find that when applying both multi-sampling and McRay, the deviation value was similar compared with applying multi-sampling 5x5 only. Similarity, there are no apparent differences in the deviation trends with non-scattering-contaminated and scattering-contaminated X-ray. The result indicates that scattering contaminated X-ray had a little impact on the measurement results when measuring the radius with the use of local thresholding with the application of sub-pixel detector, which is a deepening understanding of Lifton's findings [27].

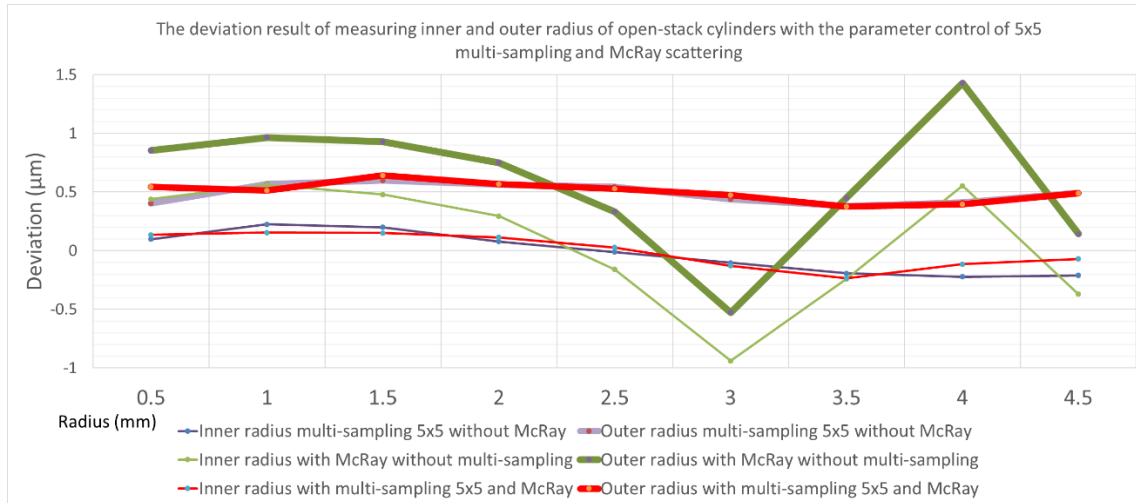


**Figure 4-18: The deviation result for the application of multi-sampling (5x5) and McRay scattering**

#### 4.2.3.4 Thickness comparison

The thickness is defined as the perpendicular distances between two adjacent planes vertical to the rotation axis on the cylinders. Each plane was defined using the Gaussian fitting protocol with around 1000 fitting points on the determined surface by the local threshold scheme, and the distances were measured by using measurement tool calculating the vertical distance between two adjacent

planes. The measurement was conducted under all six scanning conditions (shown in Table 3-4).

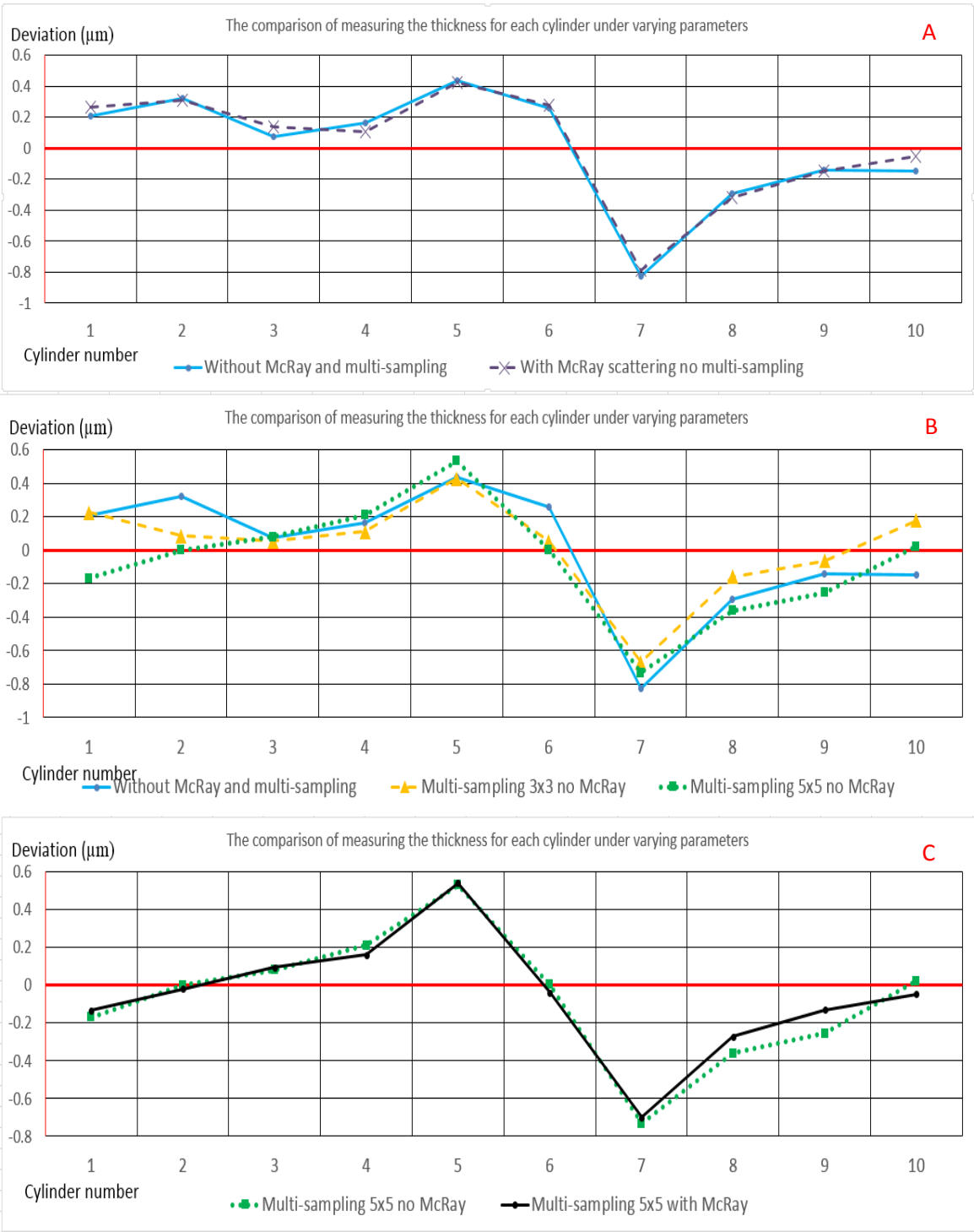


**Figure 4-19: The comparison of the deviation results under four scanning parameters, and each of graph represents the comparison between A. no scattering no multi-sampling, scattering no multi-sampling; B. no scattering no**

**multi-sampling, no scattering multi-sampling 3x3, no scattering multi-sampling 5x5; C. no scattering multi-sampling 5x5, scattering multi-sampling 5x5.**

Each figure in Figure 4-19 describes the comparison of measurement deviation of thickness of open stack cylinder under simulation scanning under two or three scanning parameters. The most significant deviation of  $0.8\text{ }\mu\text{m}$  (8% of the pixel size) took place for measuring the 7<sup>th</sup> cylinder under no multi-sampling no scattering. The purpose of this experiment was to identify that whether multi-sampling and scattering influenced the measuring geometry features along the rotational axis, rather than vertical to the rotational axis as the previous experiments regarding radius measurement did. An inspection of the data in Figure 4-19 A and C reveals that scattering had no noticeable impact on the measurement error, and it was independent of the multi-sampling application, and in accordance with the present results, the previous study [33] have also demonstrated that scattering had no significant effect on the measurement result when using local thresholding surface determination protocol.

### 4.3 AM artefacts

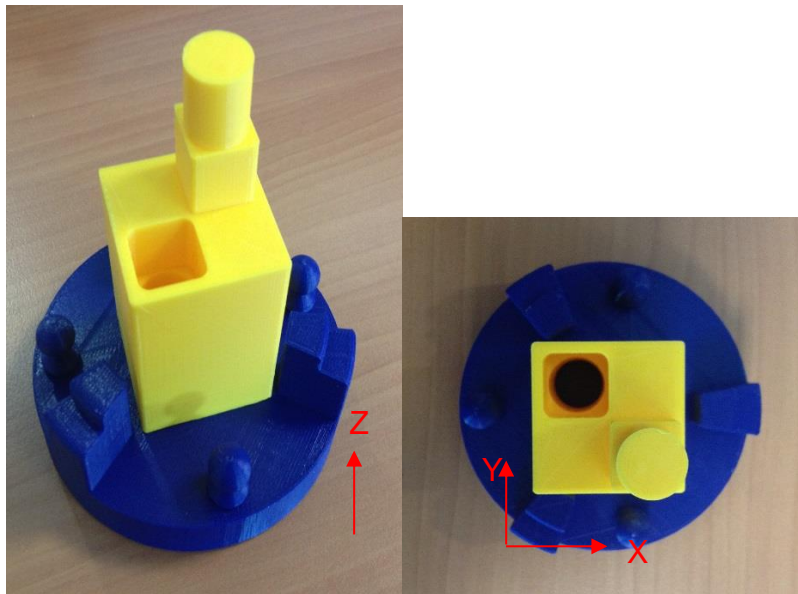


**Figure 4-20: The test sample designed by National Physical Laboratory, with positive cube and cylinder and the according negative cube and cylinder**



The sample and main testing procedures were illustrated in Section 3.3.6 and Section 0. The surface was determined by local thresholding with choosing the example of background and material manually. The measurement for positive/negative cylinders was similar as in stack cylinders, with cylinder fitting with the Gaussian fit protocol. In order to measure the distance between planes, planes were defined in Gaussian fitting by clicking 20 points on the surface, and over 1000 fitting points were generated. Each plane was defined third times in order to investigate the user impact on the measurement, and nine measurement results were obtained based on six fitted planes representing two actual planes. The measurement parts were named as follows, for instance: Cubic Neg side length X-axis represents the perpendicular distance along the X-axis between 2 planes parallel to Y-Z plane (perpendicular to X-axis) in the negative cube.

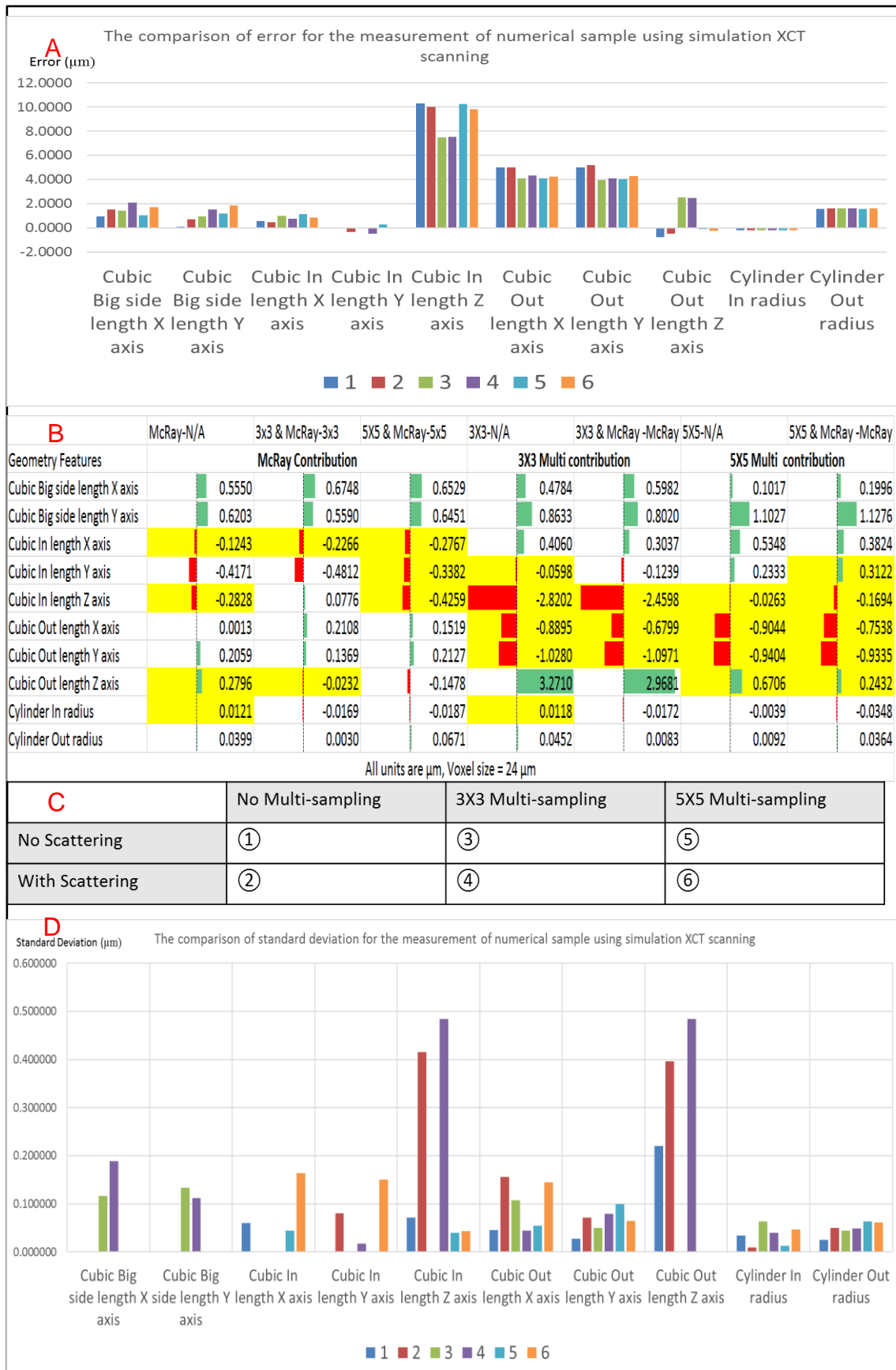


**Figure 4-21: A: The measurement error results for the sample in 6 scanning parameters for different geometry features based on the average of 9 measurement results; B: The deviation comparison with serious of subtraction, where N/A means the scanning parameter of non-scattered X-ray & no multi-sampling applied, and for example, '3x3 & McRay-McRay' means the data was acquired by subtracting the average deviation (Scattered X-ray only) from the deviation (3x3 multi-sampling & scattered X-ray), and yellow blocks indicate that under the row showing 'X-Y', the absolute value of deviation of condition X is lower than Y; C: Six scanning parameters indicated by numbers, which presents numbers in**

Figure 4-21 A and D; D: Standard deviation of the error for all 6 scanning parameters for different geometry features based on 9 individual measurements

Figure 4-21 presents the measurement deviation results for the different type of geometry features under all six scanning parameters. It is obvious to find that the deviations are different with the change of scanning parameters or the different type of geometry features to be measured.

The single most striking observation to emerge from the data comparison was the remarkably similar deviation for the measurement of inner and outer cylinders under all six scanning parameters, where the maximum deviation difference was  $0.0671\ \mu\text{m}$  which was about  $1/357$  of the voxel size when comparing 5x5 & McRay and 5x5 for the outer cylinder. The findings of this study do not support the previous research of the scanning of stack tubes, where the application of multi-sampling had a considerable impact on the measurement of cylinders.

For all geometry features, the measurement on inner cubic along the rotation axis (Z-axis in Figure 4-20) had greater deviations compared with other geometry features, and the most significant deviation was  $10.2934\ \mu\text{m}$  (42.89% of the voxel size) under multi-sampling of 5x5. Although the application of 3x3 multi-sampling detector reduced the deviation to  $7.4732\ \mu\text{m}$ , it still reached 31.1% of the voxel size, and the application of 5x5 multi-sampling detector did not have any improvement.

However, there are contrary comparison results for the measurement of the outer cube along the Z-axis, where the application of 3x3 multi-sampling deteriorated the measurement result, and 5x5 multi-sampling reduced the deviation to  $-0.1\text{ }\mu\text{m}$  (1/240 of voxel size) with non-scattered X-ray and  $-0.25\text{ }\mu\text{m}$  (1/96 of voxel size) with scattering-contaminated X-ray. These results may help us to understand that in real future scanning, an unquestioning increase of sub-pixels on the detector for multi-sampling might not lead to good measurement results.

Those findings indicate that the orientation in the distance measurement using XCT is a significant factor that should be considered, especially when measuring the distance along the rotation axis.

Figure 4-21B displays the explicit comparison of measurement errors integrating the scanning parameters and the geometry features, where yellow blocks indicate better resulting (less deviation) with applied scanning parameters. If we now turn to the scattering-contaminated X-ray contribution section, the most significant deviation change is  $0.6748\text{ }\mu\text{m}$  which is less than 1/35 of the voxel size when measuring big cube along X-axis when comparing 3x3 & McRay and 3x3. These results are in accord with the previous studies in this thesis and Lifton's [27] studies indicating the negligible influence on the measurement result.

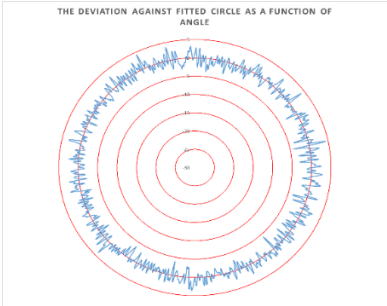
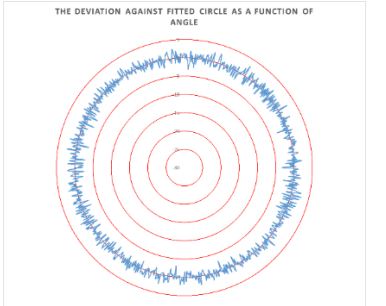
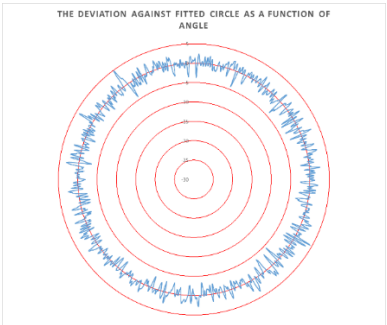
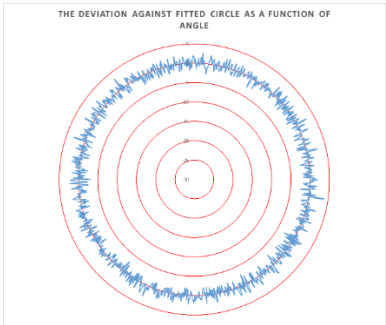
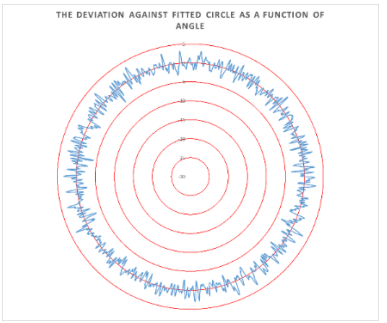
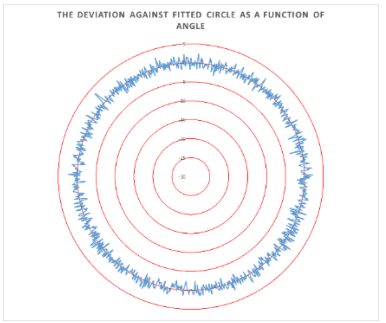
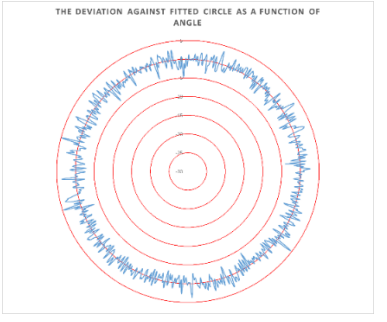
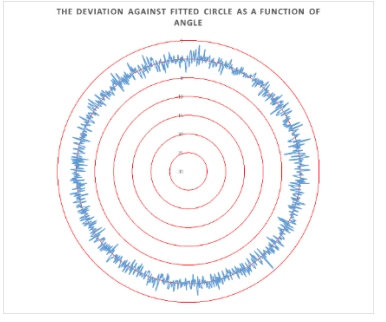
However, unlike the study results of stack tubes described before, the effect of multi-sampling correction is complex. For the application of 3x3 multi-sampling detector, in all ten geometry features, 3x3 multi-sampling reduced the deviation for five geometry features for X-rays without scattering-contamination while results for only three geometry features got improved with scattering-contaminated X-ray. However, if looking at the table cautiously, there are less than  $0.07\text{ }\mu\text{m}$  differences for inner radius and inner cube Y axis in respect to the scattering-contaminated X-ray and the difference is negligible. Except for the measurement of the outer cube in Z-axis, it is also apparent to find that the application of 3x3 multi-sampling increased the error for measurement geometry features of big cube and inner cube in X-axis, where the maximum increasing error is  $0.8633\text{ }\mu\text{m}$  (1/28 of voxel size). When looking into 5x5 multi-sampling applying, the maximum increasing error reached  $1.1276\text{ }\mu\text{m}$  (1/21 of voxel size).

Interestingly, there are opposite results for the measurement of the outer cube along the rotation axis. The application of 3x3 multi-sampling detector largely increased the measurement error by 3.271  $\mu\text{m}$  (1/7.33 of voxel size) with non-scattered X-ray and 2.9681  $\mu\text{m}$  (1/8 of voxel size) with scattering-contaminated X-ray, 5x5 multi-sampling detector reduced the error by 0.6706  $\mu\text{m}$  (1/35.8 of voxel size) for non-scattered X-ray and 0.2432  $\mu\text{m}$  (less than 1/98 of voxel size). Hence, it could conceivably be hypothesised that the geometry features could significantly influence the effect of multi-sampling detectors.

Figure 4-21D compares the standard deviation results based on nine individual measurements for each geometry features in all six scanning parameters. Most standard deviations are within 0.2  $\mu\text{m}$ , which means that in actual measurement, based on the measured average value, given a fixed surface determination protocol, the probability for the measurement results spread within the region of  $l \pm 0.2 \mu\text{m}$  would be 68.2%,  $l \pm 0.4 \mu\text{m}$  for 95.4%, and  $l \pm 0.6 \mu\text{m}$  for 99.8%. The minimum standard deviation value is  $\sigma = 8 \times 10^{-6} \mu\text{m}$ , for the measurement of the big cube in the Y-axis with the multi-sampling 5x5 detector and non-scattered X-ray. The maximum standard deviation is 0.485  $\mu\text{m}$ , in the measurement of inner cube along rotation axis with 3x3 multi-sampling detector under scattering-contaminated X-ray beams, which indicates that the measurement result could be  $l \pm 0.485 \mu\text{m} (l \pm \frac{1}{49} \text{pixel size})$  ,  $l \pm 0.97 \mu\text{m} (l \pm \frac{1}{24} \text{pixel size})$  ,  $l \pm 1.455 \mu\text{m} (l \pm \frac{1}{16} \text{pixel size})$  with the possibility of 68.2%, 95.4% and 99.8% respectively. Interestingly, the four greatest deviations are distributed in the measurement of length along the rotation axis with scattering-contaminated X-ray illumination, and with the application of 3x3 multi-sampling detector, the scattering-contaminated X-ray beam significantly increased the dispersion degree. However, the dispersion degree for the measurement of those geometry features could be reduced by the application of 5x5 multi-sampling detector, especially when considering the scattering-contaminated X-ray beams. In short, the influence of scattering-contaminated X-ray beam could amplify the consequence of human preference factors, with a given condition of the already determined surface in the software.

According to charts shown in Figure 4-21, the influence of scattering-contamination and the improvement effect of multi-sampling are complex. In order to detailly explain how those factors influence the measurement errors, it is essential to research how they changed the quality of 2D slice images considering deeply research of the 3D reconstruction process.

#### **4.4 The effect of cone beam angles**

Cone beam angle	Inner Circle	Outer Circle
0	 <p>THE DEVIATION AGAINST FITTED CIRCLE AS A FUNCTION OF ANGLE</p>	 <p>THE DEVIATION AGAINST FITTED CIRCLE AS A FUNCTION OF ANGLE</p>
1.79	 <p>THE DEVIATION AGAINST FITTED CIRCLE AS A FUNCTION OF ANGLE</p>	 <p>THE DEVIATION AGAINST FITTED CIRCLE AS A FUNCTION OF ANGLE</p>
3.58	 <p>THE DEVIATION AGAINST FITTED CIRCLE AS A FUNCTION OF ANGLE</p>	 <p>THE DEVIATION AGAINST FITTED CIRCLE AS A FUNCTION OF ANGLE</p>
5.355	 <p>THE DEVIATION AGAINST FITTED CIRCLE AS A FUNCTION OF ANGLE</p>	 <p>THE DEVIATION AGAINST FITTED CIRCLE AS A FUNCTION OF ANGLE</p>

**Table 4-1: The comparison of deviation against fitted circle in different positions within the tube as a function of cone beam angle**

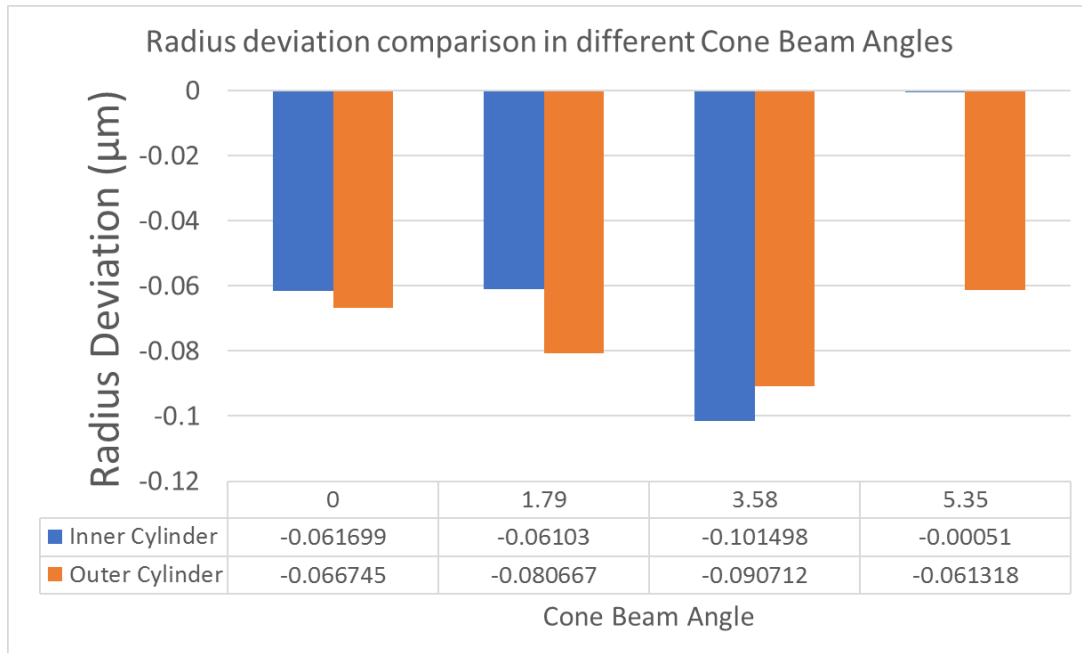


**Figure 4-22: The comparison of radius deviation against CAD model in different cone beam angles**

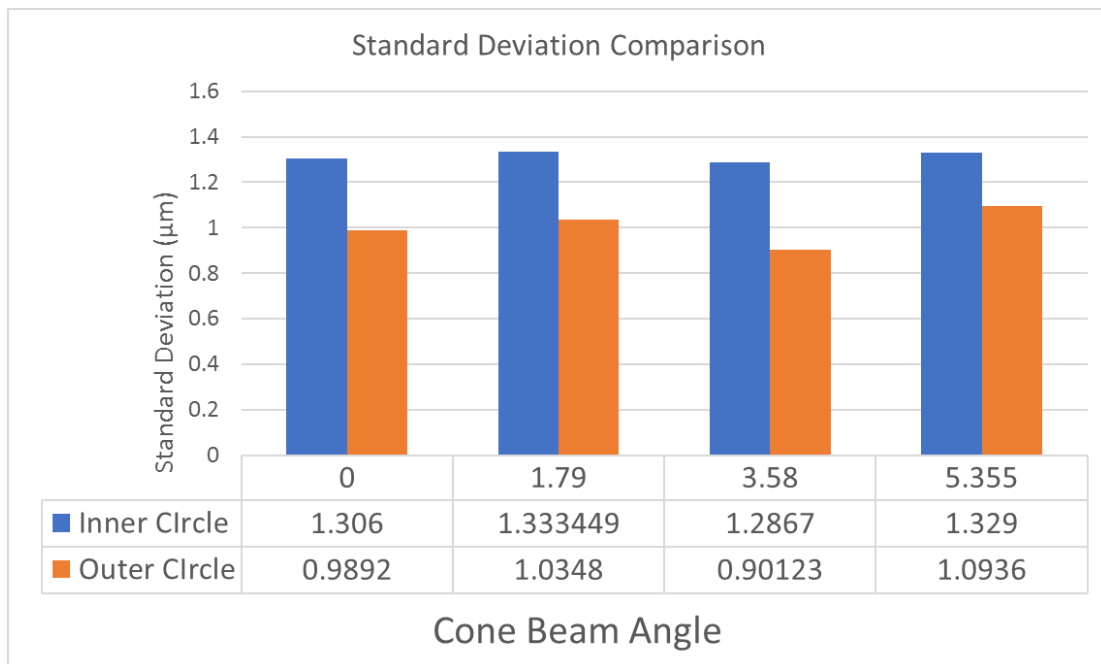


**Figure 4-23: The comparison of standard deviation value of fitting points against the fitted circle for different cone beam angles**



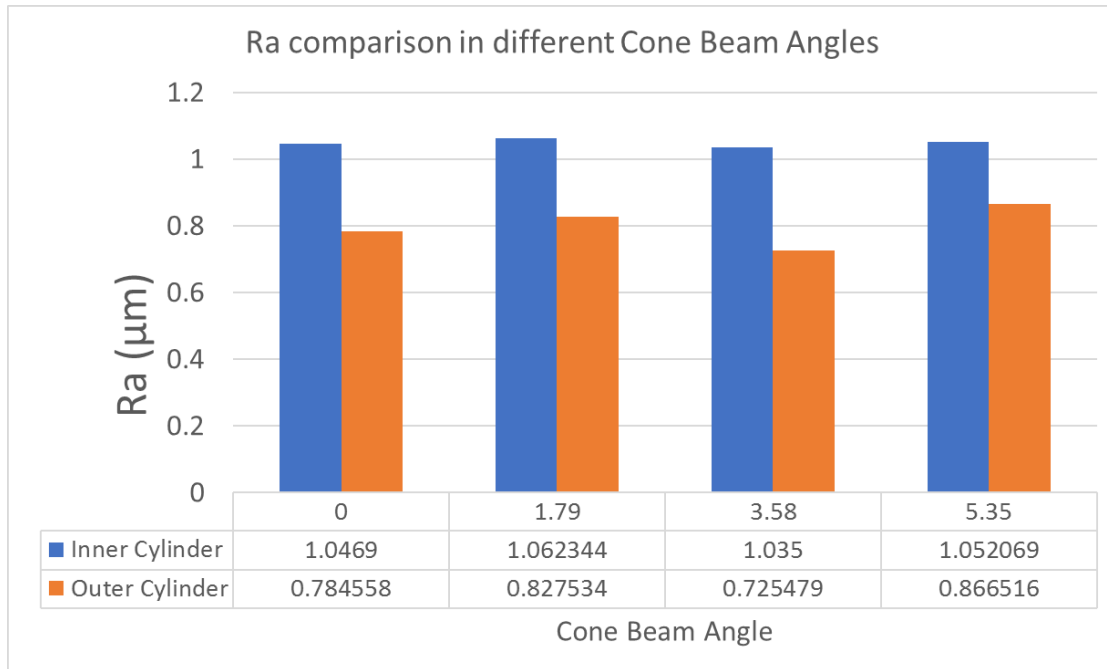


**Figure 4-24: The Ra value comparison of fitting points against the fitted circle for different cone beam angles**

Table 4-1 compares the circle fitting points on the tube (with inner cylinder and outer cylinder) against the perfect fitted circle in varying cone beam angles. Eight images in Table 4-1 is a radar diagram showing the deviations of each fitting point against the fitted circle. The radius deviation, standard deviation and Ra value are also illustrated in the table. There are no distinct differences when comparing eight radar diagrams. The explicit comparison of radius deviation is illustrated in Figure 4-22. It can be seen the positive results in the figure. The minimum radius deviation is only  $-0.00051 \mu\text{m}$ , which is only  $1/24144$  of the voxel size, and the maximum radius deviation is  $-0.1015 \mu\text{m}$ , accounting for less than  $1/131$  of voxel size, which is also the maximum change in four different cone beam angles. Figure 4-24 describes the attractive result regarding Ra value. No discernible difference is found with the change of cone beam angle. However, the Ra values for outer circle are generally less than for inner circle, which means that after the XCT simulation scanning process, the outer surface in 3D reconstructed data is smoother than the inner surface, which could indicate that the measurement of outer surface could have less probability of influence by personal preferences in the geometry determination step.

The slight differences of the measurement error among different cone beam angles could be attributed to the consideration of scale calibration in the 3D reconstruction process. In the 3D model, the reason of the generation of smoother outer surface is still unknown, and further investigation could start from 2D slices containing inner and outer surfaces to be reconstructed.

## 5 Conclusion

This study set out to develop simulation data for soft gauge purposes using simulation scanning. The aim of the present research was to examine the influence of scattering-contaminated X-ray, voltage and current on the measurement error by 2D simulation scanning and testing the influence factor of multi-sampling property of the detector, scattering-contaminated X-ray, geometry features and cone-beam angles.

This study has shown that:

- When using local threshold surface determination scheme, the scattering contamination had limited on the measurement result (up to 1/35 of voxel size), but it could magnify the influence of human factors.
- The improvement effect of the application of multi-sampling detectors may vary depending on the type of geometry features to be measured.
- Cone beam angle had no obvious influence on the measurement result.
- The extent of influence of human preference was largely depended on the geometry features, orientations, scattering-contaminated X-ray beams and multi-sampling detectors.

The findings of this research provide insights for the error sources in the XCT dimensional measurement. A key strength of the present study was the sufficient comparison of the combination of scanning parameters.

A number of limitations need to be noted regarding the present study.

- One issue with the current study was that all numerical samples were set the material as the aluminium, which could limit the expand of the conclusion regarding the scattering contamination.
- This study is limited by the selection of only aluminium.
- In addition, it is unfortunate that the study did not include the evaluation of personal preference in the surface determination step, and all assumption and conclusion concerning the personal preference are only valid under the condition of existing given surface determination. One source of

weakness in this study which could have affected the measurements by XCT simulation was the personal habit in the surface determination.

This research has thrown up many questions in need of further investigation. For example, how multi-sampling detector affected the 2D images, then affected 3D model; why the positive or negative sign of deviation could vary; why scattering contamination could increase the standard deviation, etc

Future studies should explore the effects of the material (single or multiple material). In addition, more research is needed to develop a deeper understanding of the relationships between the influencing factors and the measurement deviation with support from the simulation data. In further research, the improvement by the application of multi-sampling to different geometry features could be explored with specific data support.

## 6 References

1. Wellington SL., Vinegar HJ. X-Ray Computerized Tomography. Journal of Petroleum Technology. Society of Petroleum Engineers; 1 August 1987; 39(08): 885–898. Available at: DOI:10.2118/16983-PA
2. Hounsfield GN. Computerized transverse axial scanning (tomography): Part 1. Description of system. The British Journal of Radiology. The British Institute of Radiology ; 28 December 1973; 46(552): 1016–1022. Available at: DOI:10.1259/0007-1285-46-552-1016
3. Kalender WA. X-ray computed tomography. Physics in Medicine & Biology. IOP Publishing; 2006; 51(13): R29.
4. Kruth JP., Bartscher M., Carmignato S., Schmitt R., De Chiffre L., Weckenmann A. Computed tomography for dimensional metrology. CIRP Annals - Manufacturing Technology. 2011; 60(2): 821–842. Available at: DOI:10.1016/j.cirp.2011.05.006
5. Reimers P., Goebbels J. New possibility of nondestructive evaluation by X-Ray computed tomography. 1983; Available at: <https://opus4.kobv.de/opus4-bam/frontdoor/index/index/docId/40698>
6. Sun W., Beown SB., Leach RK. An overview of industrial X-ray computed tomography. National Physical Laboratory; 2012.
7. Klug HP., Alexander LE. X-ray diffraction procedures: for polycrystalline and amorphous materials. X-Ray Diffraction Procedures: For Polycrystalline and Amorphous Materials, 2nd Edition, by Harold P. Klug, Leroy E. Alexander, pp. 992. ISBN 0-471-49369-4. Wiley-VCH, May 1974. 1974; : 992.
8. Judy PF. The line spread function and modulation transfer function of a computed tomographic scanner. Medical Physics. Wiley-Blackwell; 1 July 1976; 3(4): 233–236. Available at: DOI:10.1118/1.594283
9. NDT. Attenuation Coefficient. Available at: <https://www.nde-ed.org/EducationResources/CommunityCollege/Radiography/Physics/attenuationCoef.htm>
10. McNaught AD., Wilkinson A., International Union of Pure and Applied Chemistry. Compendium of chemical terminology : IUPAC recommendations. Blackwell Science; 1997. 450 p. Available at: <http://www.old.iupac.org/publications/books/author/mcnaught.html>
11. A reference sample for investigating the stability of the imaging system of x-ray computed tomography. Available at: <http://iopscience.iop.org/article/10.1088/0957-0233/27/8/085004/pdf>
12. Patterson BM., Hamilton CE. Dimensional Standard for Micro X-ray Computed Tomography. Available at: DOI:10.1021/ac101522q
13. Garboczi EJ. Three-dimensional mathematical analysis of particle shape using X-

- ray tomography and spherical harmonics: Application to aggregates used in concrete. *Cement and Concrete Research*. Pergamon; 1 October 2002; 32(10): 1621–1638. Available at: DOI:10.1016/S0008-8846(02)00836-0
14. Bartscher M., Hilpert U., Härtig F., Neuschaefer-Rube U., Goebbels J., Staude A. Industrial computed tomography, an emerging coordinate measurement technology with high potentials. *Proc. of NCSL International Workshop and Symposium*. 2008. pp. 3–7.
  15. Mitchell KW. A generalized approach to wall thickness measurements in CT images. *Topical Proc. Industrial Computerized Tomography, ASNT*. 1989; : 120–124.
  16. Carmignato S., Savio E., Symposium LDC-P of 2nd I., 2004 undefined. CT techniques for reconstructing 3D geometrical models of complex parts: an approach for traceability establishment and uncertainty evaluation. *researchgate.net*. Available at: [https://www.researchgate.net/profile/Simone\\_Carmignato/publication/308612114\\_CT\\_techniques\\_for\\_reconstructing\\_3D\\_geometrical\\_models\\_of\\_complex\\_parts\\_an\\_approach\\_for\\_traceability\\_establishment\\_and\\_uncertainty\\_evaluation/links/57e8d3b908aed7fe466be001.pdf](https://www.researchgate.net/profile/Simone_Carmignato/publication/308612114_CT_techniques_for_reconstructing_3D_geometrical_models_of_complex_parts_an_approach_for_traceability_establishment_and_uncertainty_evaluation/links/57e8d3b908aed7fe466be001.pdf)
  17. Werth Messtechnik (2011). Available at: [www.werth.de/de/unser-angebot/](http://www.werth.de/de/unser-angebot/)
  18. Kiekens K., Tan Y., Kruth J-P., Voet A., Dewulf W. Parameter dependent thresholding for dimensional X-ray computed tomography. Available at: [https://lirias.kuleuven.be/bitstream/123456789/314753/1/Kiekens\\_Final.pdf](https://lirias.kuleuven.be/bitstream/123456789/314753/1/Kiekens_Final.pdf)
  19. Desplentere F., Lomov SV., Woerdeman DL., Verpoest I., Wevers M., Bogdanovich A. Micro-CT characterization of variability in 3D textile architecture. *Composites Science and Technology*. October 2005; 65(13): 1920–1930. Available at: DOI:10.1016/j.compscitech.2005.04.008
  20. Izzo JR., Joshi AS., Grew KN., Chiu WKS., Tkachuk A., Wang SH., et al. Nondestructive Reconstruction and Analysis of SOFC Anodes Using X-ray Computed Tomography at Sub-50 nm Resolution. *Journal of The Electrochemical Society*. 2008; 155(5): B504. Available at: DOI:10.1149/1.2895067
  21. Kiekens K., Welkenhuyzen F., Tan Y., Bleys P., Voet A., Kruth J-P., et al. A test object with parallel grooves for calibration and accuracy assessment of industrial computed tomography (CT) metrology. *Measurement Science and Technology*. IOP Publishing; 1 November 2011; 22(11): 115502. Available at: DOI:10.1088/0957-0233/22/11/115502
  22. Müller P., Hiller J., Dai Y., Andreasen JL., Hansen HN., De Chiffre L. Estimation of measurement uncertainties in X-ray computed tomography metrology using the substitution method. *CIRP Journal of Manufacturing Science and Technology*. Elsevier; 1 January 2014; 7(3): 222–232. Available at: DOI:10.1016/J.CIRPJ.2014.04.002

23. Flay N., Sun W., Brown S., Leach R., Blumensath T. Investigation of the focal spot drift in industrial cone-beam X-ray computed tomography. Proceedings of the DIR. 2015;
24. Corcoran HC., Brown SB., Robson S., Speller RD., McCarthy MB. OBSERVATIONS ON THE PERFORMANCE OF X-RAY COMPUTED TOMOGRAPHY FOR DIMENSIONAL METROLOGY. ISPRS - International Archives of the Photogrammetry, Remote Sensing and Spatial Information Sciences. 15 June 2016; XLI-B5: 25–31. Available at: DOI:10.5194/isprs-archives-XLI-B5-25-2016
25. Bewoor AK., Kulkarni VA. Metrology & measurement. 2009. 558 p. Available at: <http://www.worldcat.org/title/metrology-measurement/oclc/879567943>
26. Alvarez RE., Macovski A. Energy-selective reconstructions in X-ray computerised tomography. Physics in Medicine and Biology. IOP Publishing; 1 September 1976; 21(5): 002. Available at: DOI:10.1088/0031-9155/21/5/002
27. Lifton JJ., Malcolm AA., McBride JW. Simulating the influence of scatter and beam hardening in dimensional computed tomography Related content An experimental study on the influence of scatter and beam hardening in x-ray CT for dimensional metrology. Meas. Sci. Technol. 2017; 28. Available at: <http://iopscience.iop.org/article/10.1088/1361-6501/aa80b2/pdf>
28. Hiller J., Maisl M., Reindl LM. Uncertainty in measurement for x-ray-computed tomography using calibrated work pieces Related content Physical characterization and performance evaluation of an x-ray micro-computed tomography system for dimensional metrology applications. Available at: <http://iopscience.iop.org/article/10.1088/0957-0233/21/5/054008/pdf>
29. Teeter MG., Kopacz AJ., Nikolov HN., Holdsworth DW. Metrology test object for dimensional verification in additive manufacturing of metals for biomedical applications. J Engineering in Medicine. 2015; 229(1): 20–27. Available at: DOI:10.1177/0954411914565222
30. Affenzeller C., Gusenbauer C., Reiter M., Kastner J. Measurement uncertainty evaluation of an X-ray computed tomography system. Available at: [http://www.ndt.net/events/DIR2015/app/content/Paper/7\\_Gusenbauer\\_Rev1.pdf](http://www.ndt.net/events/DIR2015/app/content/Paper/7_Gusenbauer_Rev1.pdf)
31. du Plessis A., Rossouw P. X-ray computed tomography of a titanium aerospace investment casting. Case Studies in Nondestructive Testing and Evaluation. Elsevier; 1 April 2015; 3: 21–26. Available at: DOI:10.1016/J.CSNDT.2015.03.001
32. Kraemer A., Lanza G. Assessment of the Measurement Procedure for Dimensional Metrology with X-ray Computed Tomography. Procedia CIRP. Elsevier; 1 January 2016; 43: 362–367. Available at: DOI:10.1016/J.PROCIR.2016.02.018
33. Lifton JJ., Malcolm AA., McBride JW. An experimental study on the influence of scatter and beam hardening in x-ray CT for dimensional metrology. Measurement Science and Technology. IOP Publishing; 1 January 2016; 27(1): 015007. Available

at: DOI:10.1088/0957-0233/27/1/015007

34. Kathryn M., Chiffre D., Stolfi A., Kathryn Thompson M., Carli L., De Chiffre L. Quantifying the Contribution of Post-Processing in Computed Tomography Measurement Uncertainty. *Procedia CIRP*. 2016; 43: 297–302. Available at: DOI:10.1016/j.procir.2016.02.123
35. Canny JF. Finding edges and lines in images. Massachusetts Institute of Technology. Artificial Intelligence Laboratory. Technical Report AI-TR-72983. 1983;
36. Townsend A., Pagani L., Blunt L., Scott PJ., Jiang X. Factors affecting the accuracy of areal surface texture data extraction from X-ray CT. *CIRP Annals*. Elsevier; 1 January 2017; 66(1): 547–550. Available at: DOI:10.1016/J.CIRP.2017.04.074
37. Carmignato S., Dreossi D., Mancini L., Marinello F., Tromba G., Savio E. Testing of x-ray microtomography systems using a traceable geometrical standard. *Measurement Science and Technology*. IOP Publishing; 1 August 2009; 20(8): 084021. Available at: DOI:10.1088/0957-0233/20/8/084021
38. Moylan S., Slotwinski J., Cooke A., Jurrens K., Donmez MA. An Additive Manufacturing Test Artifact. *Journal of research of the National Institute of Standards and Technology*. National Institute of Standards and Technology; 2014; 119: 429–459. Available at: DOI:10.6028/jres.119.017
39. Moylan S., Slotwinski J., Cooke A., Jurrens K., Alkan Donmez M. PROPOSAL FOR A STANDARDIZED TEST ARTIFACT FOR ADDITIVE MANUFACTURING MACHINES AND PROCESSES. Available at: [https://ws680.nist.gov/publication/get\\_pdf.cfm?pub\\_id=911953](https://ws680.nist.gov/publication/get_pdf.cfm?pub_id=911953)
40. Sun W., Brown S., Woolliams P., McCarthy M., White J., Attallah M. Applications and systematic errors of X-ray computed tomography associated with dimensional metrology.
41. Möhring H-C., Kersting P., Carmignato S., Yagüe-Fabra JA., Maestro M., Jiménez R., et al. A Testpart for Interdisciplinary Analyses in Micro Production Engineering. *Procedia CIRP*. Elsevier; 1 January 2015; 28: 106–112. Available at: DOI:10.1016/J.PROCIR.2015.04.018
42. Mahesh M., Wong YS., Fuh JYH., Loh HT. Benchmarking for comparative evaluation of RP systems and processes. *Rapid Prototyping Journal*. Emerald Group Publishing Limited; 2004; 10(2): 123–135.
43. Castillo L. Study about the rapid manufacturing of complex parts of stainless steel and titanium. TNO report with the collaboration of AIMME. 2005;
44. Probst G., Boeckmans B., Kruth J-P., Dewulf W. Compensation of drift in an industrial computed tomography system. 2016; Available at: [www.3dct.at](http://www.3dct.at)
45. International Symposium on Digital Industrial Radiology and Computed Tomography 2011 Berlin F., Deutsche Gesellschaft für Zerstörungsfreie Prüfung



W., International Symposium on Digital Industrial Radiology and Computed Tomography (DIR-CT) (2011 2011.06.20-22 Berlin) A., Kruth J-P., Dewulf W. International Symposium on Digital Industrial Radiology and Computed Tomography : June 20 - 22, 2011, Berlin, Germany. DGZfP; 2011. Available at: <https://lirias.kuleuven.be/handle/123456789/333023>

46. NIST Additive Manufacturing Test Artifact | NIST. Available at: <https://www.nist.gov/el/intelligent-systems-division-73500/production-systems-group/nist-additive-manufacturing-test>



